electronics

MDPI

Article

Research on Driving Characteristics of Three-Chamber Pneumatic Bellows Soft Actuator for Wall-Climbing Robots

Liujia Yang [1], Laixi Zhang [1,2,*] and Fengshan Su [3]

[1] School of Mechanical and Electrical Engineering, Lanzhou University of Technology, Lanzhou 730050, China
[2] Key Laboratory of Intelligent Integration Technology for Complete Equipment, Ministry of Education, Lanzhou 730050, China
[3] The Qingdao Research Institute, Northwestern Polytechnical University, Qingdao 266200, China
* Correspondence: laixi_zh@163.com

Abstract

To overcome the limitations of existing pneumatic soft actuators, a three-chamber pneumatic bellows soft actuator was designed for soft wall-climbing robots. Based on the constant-curvature assumption and Euler–Bernoulli beam theory, a three-parameter decoupled mechanical model was established to describe axial elongation, bending direction, and bending angle. The model reveals the mechanism by which the bending direction is independently controlled by the pressure ratio among the three chambers. Finite element analysis was employed for structural parameter optimization, identifying the optimal configuration that achieves both high displacement-stress efficiency and excellent linearity: two-layer bellows, 20 mm length, and low-hardness YG-G15 material. Experimental analysis shows that under optimal configuration conditions, the actuator can achieve continuously controllable bending and elongation motion at 0.01–0.04 MPa. Compared to the predicted values from the theoretical model, the maximum relative error in the bending angle is 14%, and the maximum relative error in the elongation is 12.5%. The study validates the accuracy of the mechanical model and provides important design guidance for pneumatic drive systems in soft wall-climbing robots.

Keywords: pneumatic soft actuator; three-chamber bellows; mechanical model; driving characteristics; wall-climbing robot

1. Introduction

In recent years, soft robots have demonstrated broad application prospects in precision grasping and complex environment exploration owing to their inherent compliance and flexibility [1]. Among various actuation methods, pneumatic actuators have become a dominant actuation technology in this field due to their low cost, lightweight design, fast response speed, and ease of control [2,3]. Single-chamber actuators typically can only achieve single-directional deformation within fixed planes. In contrast, multi-chamber structures offer superior scalability and degrees of freedom in motion control. Building on this foundation, researchers have conducted extensive investigations: Inspired by elephant trunk muscle fibers, Guan et al. [4] constructed a composite structure of braided tubes and reinforced frameworks, and designed a multi-degree-of-freedom robotic arm based on a unified kinematic model; Connolly et al. [5] controlled actuator deformation by varying fiber angles, but noted that friction between external constraint structures induces hysteresis effects, and the embedding precision of external constraint structures directly affects deformation performance; Colucci et al. [6] proposed a pneumatic actuator with antagonistic

Check for updates

Academic Editors: Yong-Tae Kim and Mahmut Reyhanoglu

Received: 14 July 2026
Revised: 25 August 2026
Accepted: 3 September 2026
Published: 27 October 2026

Copyright: © 2026 by the authors. Licensee MDPI, Basel, Switzerland. This article is an open access article distributed under the terms and conditions of the Creative Commons Attribution (CC BY) license.

air chambers composed of bellows, achieving bidirectional linear motion and completing experimental validation; and Ranzani et al. [7] introduced biomimetic pneumatic soft manipulators into minimally invasive surgery, enabling flexible movement and precise positioning of instruments within human body cavities. Additionally, soft manipulators composed of flexible joints have also demonstrated advantages in delicate grasping and operation in constrained environments [8], providing valuable insights for the study of soft actuators.

Facing complex three-dimensional curved surface environments, traditional rigid robots face severe challenges in maintaining reliable adhesion and locomotion compliance on offshore structures such as ship hulls and wind turbine towers [9,10]. Specifically, when deploying climbing robots for such inspection tasks, the flexible joints serving as the core executive components face three concrete, unresolved bottleneck challenges:

1. Surface Conformity and Adhesion Failure: Steel plates of ship hulls and turbine towers are characterized by doubly-curved geometries, weld seams, rust patches, and rivets. Traditional rigid mechanisms cannot conform to these local irregularities, leading to contact-area loss and catastrophic adhesion failure. Compliant soft joints are required to provide passive adaptability, allowing the adhesion modules to remain parallel to and in contact with the variable wall [11,12].
2. Kinematic Coupling and Control Complexity: During wall-climbing locomotion, the robot must independently regulate its stride length (for forward velocity) and steering direction (for path correction). However, existing multi-chamber soft joints typically couple axial elongation and bending in a highly nonlinear manner. This coupling forces gait planning to rely on computationally expensive, iterative numerical solvers or look-up tables rather than closed-form, real-time control laws [13].
3. Payload and Pressure Constraints: Mobile climbing platforms are strictly payload-limited, carrying small, low-power onboard micro-compressors. This requires the joint actuators to achieve sufficient elongation and bending angles under low pressures (typically below 0.04 MPa) to minimize energy consumption and onboard weight [14].

Therefore, developing a soft-joint actuator capable of low-pressure, three-dimensional omnidirectional bending and fully decoupled axial elongation is of paramount engineering importance to advance the surface adaptability and motion flexibility of climbing robots.

To address these systemic bottlenecks, previous researchers have made extensive efforts, yet critical technical blanks remain unfilled.

Regarding surface conformity (Challenge 1), traditional climbing platforms have heavily relied on passive spring-damper suspensions or active micro-alignment linkages [9,10]. While these rigid-body solutions improve contact, they significantly increase the robot's dead weight and mechanical complexity. Soft actuators have emerged as an elegant alternative due to their inherent structural compliance [1,11]. However, when conventional soft actuators (such as pneu-nets or fiber-reinforced tubes) are deployed as compliant joints, they often lack sufficient load-bearing capacity and directional stiffness, making them prone to structural buckling under the robot's gravity [12]. Thus, achieving highly compliant wall-conformity without sacrificing structural load-bearing rigidity remains an active blank.

Regarding kinematic decoupling (Challenge 2), multi-chamber soft structures have been developed to achieve spatial motion. However, their axial elongation (governing stride) and bending (governing steering) are intrinsically coupled in a highly nonlinear fashion [4,5]. To control such coupled systems, existing works have mostly resorted to numerical Jacobian iterations, neural-network-based empirical approximations, or dense experimental look-up tables [2]. While precise, these methods bypass the fundamental physics and are computationally heavy, preventing real-time control on resource-constrained onboard microcontrollers. A closed-form, mathematically decoupled analytical model that

maps pressure directly to spatial posture for bellows-type joints remains a significant blank in prior literature [6].

Regarding payload and pressure constraints (Challenge 3), bellows-type actuators are recognized for their superior force-to-weight ratio. However, most existing designs utilize thick, multi-layer walls or high-hardness elastomers to prevent radial expansion under pressure, which elevates the required initiation pressure well beyond the capability of lightweight onboard micro-compressors. A quantitative design space exploration that jointly optimizes wall layers and length to maximize displacement-stress efficiency under low-pressure limits (below 0.04 MPa) has not been systematically established.

To address these limitations and meet the practical application needs of wall-climbing robots, a three-chamber pneumatic bellows soft actuator has been proposed, with systematic theoretical modeling, finite element analysis, and experimental verification.

The remainder of this paper is organized as follows. Section 2 presents the structural design of the three-chamber pneumatic bellows soft actuator and establishes the decoupled mechanical model relating axial elongation, bending direction, and bending angle to the chamber pressures. Section 3 investigates the actuator's driving characteristics through finite element analysis, examining the effects of bellows layer number, actuator length, and material hardness on performance, and determines the optimal structural parameters. Section 4 describes the fabrication of the actuator prototype and the pneumatic control experimental platform, and validates the theoretical and simulation results through comparative experimental analysis of axial elongation and bending angle. Section 5 discusses the limitations of the current work and outlines directions for future research. Section 6 provides the conclusions.

To fill these gaps and meet the practical application needs of wall-climbing robots, this paper proposes a three-chamber pneumatic bellows soft actuator, together with systematic theoretical modeling, finite element analysis, and experimental verification under dry (on-land) conditions. The main contributions, organized to address the three challenges and their corresponding gaps identified above, are as follows:

(1) Developed a decoupled kinematic model for symmetric three-chamber bellows joints (addressing the gap in Challenge 2). Unlike prior multi-chamber actuators, where coupling between elongation and bending is handled through composite mechanical constraints or structure-specific empirical characterization rather than a general closed-form relationship, this study establishes a three-parameter decoupled mechanical model, encompassing axial elongation, bending direction, and bending angle. Derived from the constant-curvature assumption and Euler–Bernoulli beam theory, with the bending-direction expression and moment-arm formulation corrected for coordinate self-consistency.

(2) A closed-form pressure-to-direction mapping enabling real-time steering (addressing the gap in Challenge 2). The analytical relationship between the three-chamber pressure ratio and the bending-direction angle is studied, allowing the actuator's steering direction to be computed directly from chamber pressures without iterative numerical solving or empirical look-up tables—closing the gap between physics-based modeling and the real-time control needs of gait planning identified above.

(3) A joint safety–efficiency evaluation framework for structural parameter selection (addressing the gap in Challenge 3). Rather than evaluating structural parameters (bellows layer number, length, material hardness) individually, as in prior work, a safety factor and a displacement-stress efficiency index are defined together up front and applied jointly, providing a quantitative, comparable basis for co-optimizing structural safety and driving efficiency under the low-pressure constraints (0.01–0.04 MPa) required by lightweight, onboard-compressor-driven climbing robots.

(4) Structural optimization and experimental validation of a joint that balances compliance and load-bearing capacity (addressing the gaps in Challenges 1 and 3). Based on finite element simulation and physical-prototype testing across candidate bellows layer numbers, lengths, and material hardness, the optimal configuration (two-layer bellows, 20 mm length, YG-G15 silicone) is identified and validated, achieving continuously controllable, low-pressure elongation and bending with sufficient structural safety margin—demonstrating that passive wall-conformity and load-bearing rigidity, previously treated as a trade-off in prior soft-joint designs, can be jointly satisfied in bellows structure.

In this study, "three-degree-of-freedom" refers to the three independently controllable motion parameters of the actuator's tip—axial elongation ΔL, bending-direction angle φ, and bending angle θ—rather than three independent mechanical joints in the rigid-body sense. This usage follows the constant-curvature continuum-robot convention and is used consistently throughout the paper.

2. Actuator Structure Design and Decoupled Mechanical Model

To reduce model complexity and ensure the feasibility of theoretical analysis, the following assumptions are established:

(1) The silicone material is uniform, continuous, and isotropic;
(2) The actuator deformation satisfies the constant-curvature assumption;
(3) The mass of compressed air and the effect of gravity on actuator deformation are neglected;
(4) The cross-section of the actuator remains planar during the deformation process;
(5) There is no relative slip between the air chambers, and deformation is coordinated and consistent.

The aforementioned assumptions have been widely applied in theoretical modeling research of continuum soft actuators, enabling simplified mathematical derivations while maintaining prediction accuracy.

2.1. Three-Chamber Bellows Actuator Structure and Working Principle

The overall structure of the proposed three-degree-of-freedom pneumatic soft actuator is illustrated in Figure 1 The actuator mainly consists of three external pneumatic artificial muscles, an upper air-distribution manifold, an upper end cap, and an end-effector unit. The actuator adopts a symmetric three-chamber configuration, in which the three pneumatic artificial muscles are uniformly distributed along the circumferential direction with an angular spacing of 120°. This arrangement forms a typical parallel-actuation architecture, enabling continuous bending motions in arbitrary spatial directions.

2.2. Axial Elongation Model

After compressed air is supplied to the actuator, the actuator tip deforms under the combined action of axial forces and bending moments. The axial force governs the elongation of the actuator, whereas the resultant moment generated at the end cap determines the bending angle and bending direction. Figure 2 illustrates the axial elongation deformation of the actuator. R_1, R_2, and R_3 denote the three artificial muscles constituting the actuator module. In the figure, i represents the drive number.

https://doi.org/10.3390/electronics15214972

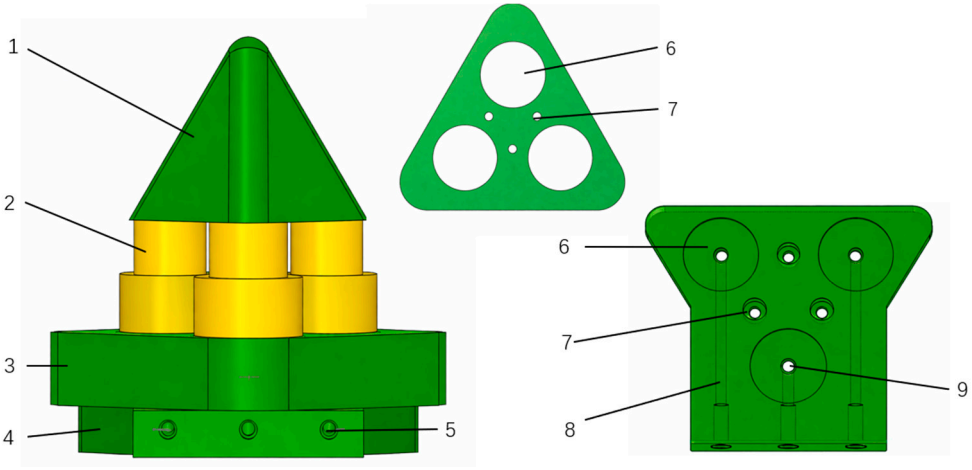


Figure 1. Structural design of the soft actuator. 1. End effector. 2. Three-degree-of-freedom artificial muscle module. 3. Upper end cap of the air duct. 4. Lower air-duct housing. 5. Pneumatic fitting mounting hole. 6. Artificial muscle mounting hole. 7. Assembly hole. 8. Control air channel. 9. Artificial muscle air inlet.

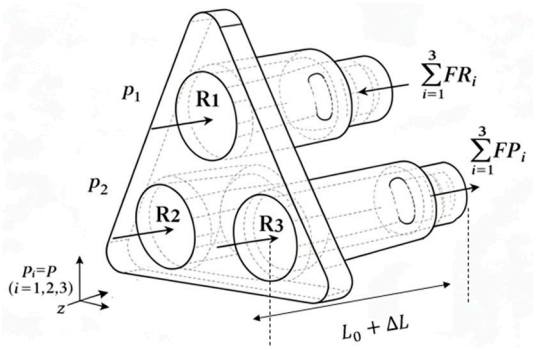


Figure 2. Analysis of the axial deformation and forces of the actuator.

After compressed air is introduced into the actuator, the inner walls of the artificial muscles expand under internal pressure, generating axial driving forces at the actuator end cap. Under the action of these forces, the actuator elongates along its longitudinal axis. During the axial deformation process, the artificial muscles develop corresponding axial strains, resulting in elastic resistance forces that oppose further elongation. In this study, the kinematic model of the actuator is established based on the constant-curvature assumption [15]. This assumption has been widely adopted in the modeling of continuum soft robots, as it significantly simplifies mathematical derivations while maintaining satisfactory prediction accuracy.

Equation (1) is a force balance on the end cap, not on an individual chamber. Because the end cap translates only along the axial direction under equal-pressure loading, the vector balance reduces to a scalar equation along z.

The static equilibrium equation of the actuator in the axial direction can be expressed as:

$$\sum_{i=1}^{3} \vec{F}_i = \sum_{i=1}^{3} \vec{F}_{Pi} - \sum_{i=1}^{3} \vec{F}_{Ri} \tag{1}$$

where

$\vec{F}_{Pi}$: denotes the pneumatic driving force generated at the actuator end cap (N);
$\vec{F}_{Ri}$: represents the elastic resistance force of the silicone material (N).

When identical pressure is applied to all three chambers ($p_1 = p_2 = p_3 = p$), the actuator extends along its central axis without directional bending. Under this condition, the axial

static equilibrium requires that the total pneumatic driving force generated by the chambers be balanced by the elastic restoring force of the silicone material. Here, $\vec{F_i}$ denotes the net axial force acting on the end cap from chamber i, defined as the difference between the pneumatic driving force and the elastic restoring force (which acts in the opposite, contractive direction): $\sum_{i=1}^{3} \vec{F_i} = \sum_{i=1}^{3} \vec{F_{Pi}} - \sum_{i=1}^{3} \vec{F_{Ri}}$. Under quasi-static equilibrium, the net force vanishes ($F_i = 0$ for each i, and hence $\Sigma \vec{F_i} = 0$), which directly yields the balance condition:

$$\sum_{i=1}^{3} \vec{F_{Pi}} = \sum_{i=1}^{3} \vec{F_{Ri}} \tag{2}$$

The axial driving force generated by an individual chamber can be expressed as:

$$\vec{F_{P_i}} = \vec{p_i} S_i \tag{3}$$

S_i is the internal cross-sectional area of chamber is bellows bore, $S_i = \frac{\pi D_2^2}{4} (\mathrm{mm}^2)$.

Based on the axial force equilibrium, the axial elongation of the actuator is obtained as:

$$\Delta L = \frac{\pi p D_2^2 L_0}{4\pi G_R (D_1^2 - D_2^2) - p\pi (D_1^2 - 2D_2^2)} \tag{4}$$

where

D_1 denotes the outer diameter of the pneumatic chamber (mm);
D_2 denotes the inner diameter of the pneumatic chamber (mm);
L_0 denotes the initial actuator length (mm);
G_R denotes the equivalent shear modulus of the silicone material (MPa).
G_R is the equivalent shear modulus of the silicone material, which characterizes the shear resistance of the bellows structure under axial pneumatic loading. For YG-G15 silicone with a Shore hardness of 15, its relationship with the elastic modulus can be expressed as:

$$G_R = \frac{E_R}{2(1+\nu)} \tag{5}$$

where E_R is the uniaxial tensile elastic modulus of the silicone material (MPa), and ν is Poisson's ratio. In this study, the equivalent shear modulus G_R was identified through material tensile testing (MPa).

2.3. Bending Direction Analysis

When different pressures are applied to the three artificial muscles, the actuator undergoes not only axial deformation but also spatial bending induced by the resultant moment acting at its distal end, as illustrated in Figure 3. Under this condition, the bending direction of the actuator is determined by the direction of the resultant moment $\mathrm{M_g}$ at the actuator tip. Meanwhile, the artificial muscles deform synchronously with the actuator and undergo the same bending deformation.

The resultant moment vector $\vec{M_g}$ acting on the distal end cap drives spatial bending. Under the constant-curvature assumption, bending is confined to a single plane; thus, $\vec{M_i}$ lies in the X–Y plane. Here, Equation (7) defines the magnitude of each chamber's moment $\vec{M_i}$, Equation (6) represents their vector sum, and M_{gx}, M_{gy} are the cartesian projections of this vector sum. This formulation resolves any conflict between scalar magnitudes and vector components.

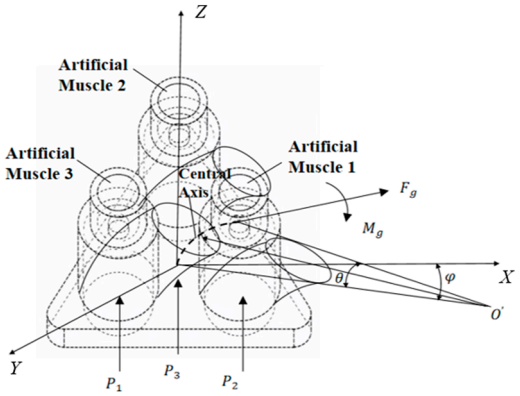


Figure 3. Bending deformation of the soft actuator.

Note that the resultant moment governing the actuator's deformation is, in general, the vector difference between the active pneumatic driving moment $\vec{M}_g$ and the passive elastic restoring moment $\vec{M}_R$ of the silicone wall. However, owing to the circumferential symmetry (120° spacing) of the three-chamber configuration and the isotropic properties of the silicone material, the bending stiffness of the joint is uniform in every direction within the X–Y plane. Consequently, whenever $\vec{M}_g$ points in a given spatial direction φ, the restoring moment $\vec{M}_g$ is guaranteed by this symmetry to act along the same line, in the opposite sense. While $\vec{M}_R$ reduces the net moment magnitude (which determines the bending angle θ, Section 2.4), it does not alter the spatial direction φ. The bending direction φ can therefore be determined from the active driving moment $\vec{M}_R$ alone, as formulated in Equation (6).

$$\vec{M}_g = \sum_{i=1}^{3} \vec{M}_i \tag{6}$$

The bending moment generated by an individual artificial muscle can be expressed as:

$$\vec{M}_i = \vec{p}_i S_i L (i = 1, 2, 3) \tag{7}$$

where L is the radial distance from the center of an individual chamber to the central axis of the actuator (mm).

Based on the moment analysis at the actuator end cap (Figure 3), the bending-direction angle of the actuator can be expressed as:

$$\varphi = atan2(\mathrm{M_{gx}}, \mathrm{M_{gy}}) \tag{8}$$

where

M_{gx} and M_{gy} denote the components of the resultant bending moment in the X- and Y-directions, respectively (N·mm).

Specifically,

$$M_{gx} = (M_2 - M_3)cos\alpha; M_{gy} = (M_2 + M_3)sin\alpha - M_1.$$

where α is the angle between the driving moment direction of an artificial muscle and the X-axis. Based on the geometric relationship shown in Figure 4, $\alpha = \frac{\pi}{6}$.

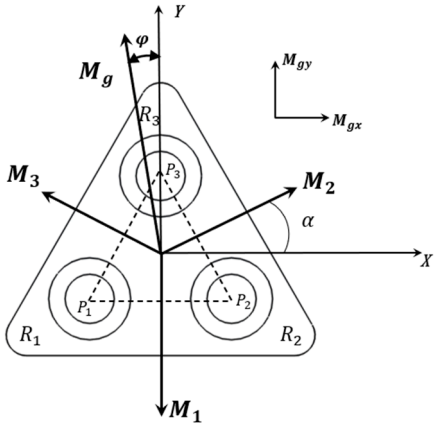


Figure 4. Bending direction of the soft actuator.

Substituting Equations (6) and (7) into Equation (8), the relationship between the bending direction and the input chamber pressures can be obtained as:

$$\varphi = atan2\left(\sqrt{3}(p_2S_2 - p_3S_3), (p_2S_2 + p_3S_3) - 2p_1S_1\right) \tag{9}$$

Figure 4 illustrates the bending directions of the three-chamber pneumatic bellows actuator under different chamber pressurization configurations. The actuator consists of three chambers symmetrically distributed along the circumferential direction, with an angular spacing of 120° between adjacent chamber centers. When a single chamber is pressurized, the actuator expands and elongates while bending toward the opposite side, with the bending direction oriented away from the pressurized chamber. When two chambers are simultaneously pressurized, the bending direction is determined by the resultant pneumatic force generated by the two chambers, and the bending plane coincides with the angular bisector plane formed by their central axes. These observations indicate that continuous control of the bending direction can be achieved within a certain range by regulating the pressurization combinations and pressure ratios of the three chambers.

When different pressures are applied to the three artificial muscles, the actuator is capable of bending in different spatial directions. The resistance to bending deformation arises from the elastic resisting moments generated by the artificial muscles, denoted as M_{Ri} (N·mm).

According to the bending moment equilibrium of the actuator, the following relationship can be obtained:

$$\sum_{i=1}^{3} M_i = \sum_{i=1}^{3} M_{Ri} \tag{10}$$

Under pneumatic actuation, the actuator bends about the neutral layer, and the distances between the artificial muscles and the neutral layer are illustrated in Figure 5.

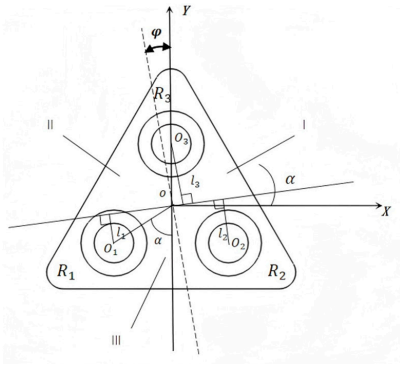


Figure 5. Distance between the artificial muscle and the neutral layer.

Owing to the symmetric arrangement of the three artificial muscles, the bending behavior of the actuator is identical within the three equally partitioned regions (Regions I, II, and III).

The deformation states of the artificial muscles for bending directions within

$$0 \le \varphi \le \frac{2\pi}{3}$$

can be described as follows:

$$0 \le \varphi \le \frac{\pi}{6}$$

artificial muscles R_2 and R_3 elongate, while R_1 contracts;

$$\frac{\pi}{6} < \varphi \le \frac{\pi}{2}$$

artificial muscle R_3 elongates, whereas R_1 and R_2 contract;

$$\frac{\pi}{2} < \varphi \le \frac{2\pi}{3}$$

artificial muscles R_1 and R_2 elongate, while R_3 contracts.

The bending direction depends solely on the relative pressure ratios among the three chambers, providing a theoretical basis for the decoupled control of chamber pressures. By continuously adjusting the bending-direction angle φ, the actuator can achieve continuous bending deformation in arbitrary spatial directions.

2.4. Bending Angle Analysis

The magnitude of the driving moment along the bending direction φ is obtained by projecting each chamber's moment onto φ: $|M_{driver}| = \sum_{i=1}^{3} p_i S_i r_i$, where $r_i = R_{at} cos(\beta_i - \varphi)$ is chamber i is moment arm relative to the bending axis, using the same chamber azimuth angles β_i ($\beta_1 = 270°$, $\beta_2 = 30°$, $\beta_3 = 150°$), defined in Section 2.3, rather than the generic index-based angle $\frac{2\pi(i-1)}{3}$ used in the original submission, which does not correspond to the actuator's actual physical layout.

The bending angle θ of the actuator is determined by the torque equilibrium between the active driving moment M_{driver} and the passive elastic bending resistance moment M_{R} of the silicone structure.

Physically, the active driving moment M_{driver} is the projection of the resultant driving moment vector $\vec{M}_g$ (defined in Section 2.3) onto the bending plane specified by the direction angle φ Defining $\vec{u}_\varphi = \cos\varphi \cdot \vec{i} + \sin\varphi \cdot \vec{j}$ as the unit vector of the bending plane, the driving moment is formulated as the dot product:

$$M_{\mathrm{driver}} = \vec{M}_g \, \vec{u}_\varphi$$

Since φ is strictly defined as the azimuthal angle of the resultant vector $\vec{M}_g$ itself (Equation (9)), this projection is mathematically equivalent to the vector magnitude $|\vec{M}_g|$ and is inherently non-negative ($M_{\mathrm{driver}} \ge 0$) under any general, arbitrary pressure combination (p_1, p_2, p_3):

$$\vec{M}_g \cdot \vec{u}_\varphi = |\vec{M}_g| \cos(0) = |\vec{M}_g| \ge 0$$

Therefore, by expanding this dot product, the driving moment can be expressed in general scalar form, without an absolute-value symbol, as:

$$M_{driver} = \sum_{i=1}^{3} p_i S_i r_i \tag{11}$$

where r_i is the distance from the center axis of the i-th chamber to the neutral bending axis.

$$r_i = R_{at}cos(\beta_i - \varphi) \tag{12}$$

Here, R_{at} is the radial distance from the centerline of each chamber to the central axis of the actuator.

The elastic bending resistance moment of the silicone material is derived based on the Euler–Bernoulli beam theory. This model has been widely validated for characterizing the bending resistance behavior of pneumatic soft actuators undergoing small to moderate deformations [16]. The derivation of the relationship between the direction of the resultant moment generated by the three chambers and the chamber pressure ratios follows the mechanical modeling approach commonly adopted for fiber-reinforced soft bending actuators [17]. For bellows-based continuum structures, the system dynamics can be systematically described within the Euler–Lagrange framework, and further dynamic extensions can be found in Ref. [18]. Accordingly, the elastic bending resistance moment of the silicone material can be expressed as:

$$M_R = \frac{\pi E_{bend}\left(D_1^4 - D_2^4\right)}{64L_0}\theta \tag{13}$$

where

M_R denotes the elastic bending resistance moment of the silicone structure (N·mm);
E_{bend} is the equivalent bending modulus of the bellows actuator (MPa).

Owing to the hollow and corrugated geometry of the bellows, the structure cannot be approximated as a solid cylindrical beam. Consequently, the equivalent bending modulus cannot be directly substituted by the bulk elastic modulus of the silicone material and was instead determined through Abaqus-based homogenization finite element analysis.

It is important to clarify why this direction-magnitude decoupling remains valid regardless of the relative magnitude of M_{driver} and M_R Owing to the actuator's structural and material symmetry, the elastic resistance moment MR depends only on the bending angle θ and is otherwise isotropic—i.e., independent of the bending-direction angle φ—since the geometric and material parameters (D_1, D_2, E_{bend}) in Equation (13) are identical for all three chambers. Consequently, MR always acts directly opposite to the bending plane in which deformation actually occurs, and equilibrium is achieved along that same plane regardless of the ratio $|M_R|/|M_{driver}|$. This isotropy assumption is itself an idealization: it neglects any configuration-dependent stiffness variation (e.g., local wall thinning or non-uniform expansion at large deformation), which is the primary reason the model's magnitude prediction (θ)—but not its direction prediction (φ)—degrades at higher pressures, as shown in Sections 4.2.3 and 4.4.

According to the moment equilibrium condition, $|M_{driver}| = M_R$, the bending angle can be expressed as:

$$\theta = \frac{64L_0\sum_{i=1}^{3} p_i S_i r_i}{\pi E_{bend}\left(D_1^4 - D_2^4\right)} \tag{14}$$

Compared with an equivalent lumped-parameter representation, the closed-form structure of this decoupled model preserves an explicit, traceable link between structural/material design parameters (bellows layer number, wall thickness, material hardness) and each individual motion channel (ΔL, φ, θ)—a link that a purely lumped stiffness/compliance matrix would not retain. This traceability directly underlies the structural parameter comparisons carried out in Section 3 and supports simplified, decoupled controller design for gait planning. The aforementioned decoupled mechanical model theoretically clarifies the control variables and coupling relationships of three motion parameters—axial

elongation, bending direction, and bending angle—respectively. However, the critical structural parameters in the model—namely, the number of bellows layers, actuator length, and silicone hardness—still require quantitative characterization of their specific effects on driving performance through simulation methods to provide reliable design guidance for the engineering design of wall-climbing robot joints. To this end, the following section systematically conducts parameter optimization research based on finite element simulation, exploring three dimensions: structural layers, length dimensions, and material hardness.

3. Analysis of Driving Characteristics and Parameter Optimization Based on Finite Element Method

3.1. Effect of Geometric Parameters on Driving Characteristics

The safety factor (SF) and displacement-stress efficiency index (η) were selected as the primary criteria for comparing layer numbers because they directly correspond to the two dominant risks a bellows joint faces under repeated low-pressure actuation: structural failure and insufficient useful output. SF quantifies the margin against material rupture or fatigue crack initiation at the fold roots—the layer number's most direct influence, since wall thickness and local stress concentration scale with layer count. η quantifies how much useful displacement is obtained per unit of stress incurred, capturing the actuator's efficiency as a joint that must repeatedly deform without accumulating excessive local strain.

Three metrics are used throughout this section to compare candidate structural configurations. Maximum von Mises equivalent stress, σ_{max}, is the peak simulated stress under a given pressure. Safety factor, $SF = \frac{\sigma_{UTS}}{\sigma_{max}}$, is the ratio of the silicone's tensile strength to the peak simulated stress, quantifying structural safety margin against material failure. Displacement-stress efficiency index, $\eta = \frac{U_{max}}{\sigma_{vmax}}$ (Equation (15)), is the output displacement obtained per unit of peak stress; a larger η means a configuration converts a given stress budget into more useful output displacement at the same pressure.

3.1.1. Effect of Bellows Layer Number

Single-layer and layer counts above three were excluded from comparison: single-layer bellows walls were found in preliminary casting trials to be prone to pinhole leaks at the fold roots under repeated pressurization, while four or more layers increase wall stiffness enough to push the required actuation pressure beyond the low-pressure range (0.01–0.04 MPa) targeted in this design. Two- and three-layer configurations therefore represent the two structurally viable candidates.

For comprehensive evaluation of the two-parameter composite driving capabilities, a displacement-stress efficiency index is introduced to reflect the single-parameter output ability per unit stress. The index is defined as:

$$\eta = \frac{U_{max}}{\sigma_{vmax}} \tag{15}$$

where U_{max} is the maximum displacement (or bending angle) output; σ_{max} is the maximum equivalent Mises stress. A larger η value indicates that a given structural configuration converts a fixed stress budget into greater useful output displacement at the same operating pressure. Note that η is derived from static (quasi-steady) finite element deformation analysis and therefore does not characterize dynamic response time or actuation speed.

To identify the optimal bellows actuator configuration for wall-climbing robotic applications, finite element simulations were conducted in Abaqus 2023 (Dassault Systèmes, France) to compare the performance of two-layer and three-layer bellows soft actuators. A pressure of 0.01 MPa was selected as the baseline operating condition. At this pressure level, both actuator configurations operate entirely within the safe working range of the silicone

material and remain in the linear deformation regime, where material nonlinearities are negligible and the finite element results can provide relatively reliable predictions.

Under the baseline pressure of 0.01 MPa, the simulation results of the two-layer and three-layer bellows actuators were comparatively evaluated from three aspects: structural strength and safety, axial actuation displacement, and overall actuation efficiency. Figure 6 presents the finite element simulation results of the two actuator configurations under the same pressure condition.

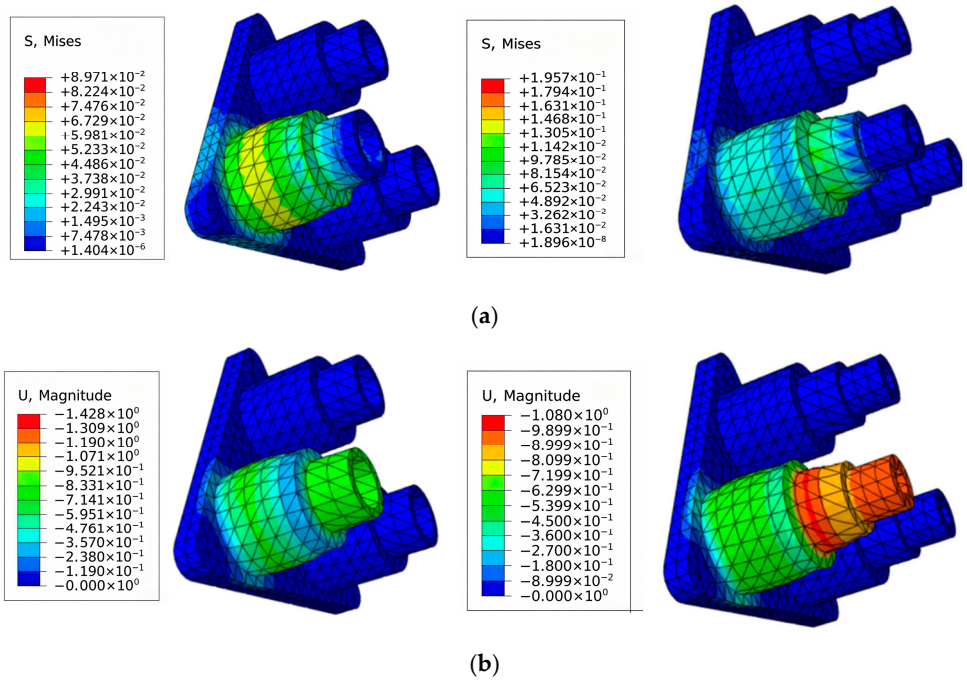


Figure 6. Finite element simulation results of two-layer and three-layer bellows actuators under the same pressure. (**a**) Comparison of equivalent stress S for actuators with different structures under the same pressure. (**b**) Comparison of equivalent displacement U for actuators with different structures under the same pressure.

The finite element modeling procedure, parameter settings, and optimization methodology adopted in this study follow the approaches commonly used in previous investigations on the structural optimization of pneumatic soft actuators [19].

(1) Strength and von Mises Stress Analysis

Under an internal pressure of 0.01 MPa, the tensile strength of the two-layer bellows silicone material is approximately: $\sigma_{UTS} \approx 3$ MPa.

The maximum von Mises equivalent stress is

$$\sigma_{max2} = 0.0897 \text{ MPa}$$

resulting in a safety factor of

$$SF_2 = \frac{3.0}{0.0897} \approx 33.44$$

Under the same loading condition, the maximum von Mises equivalent stress of the three-layer bellows structure is:

$$\sigma_{max3} = 0.1957 \text{ MPa}$$

giving a safety factor of

$$SF_3 = \frac{3.0}{0.1957} \approx 15.33$$

Figure 6a illustrates the equivalent Mises stress contours of two different structural configurations under 0.01 MPa gas pressure. The maximum equivalent stress of the two-layer bellows structure is $\sigma_{max2} = 0.0897$ MPa, with stress concentration regions primarily distributed at the junctions between bellows peaks and valleys, exhibiting relatively uniform overall distribution; the three-layer bellows structure exhibits a maximum equivalent stress of $\sigma_{max3} = 0.1957$ MPa, approximately 2.18 times that of the two-layer structure, indicating that the three-layer structure sustains higher local deformation loads under identical gas pressure, presenting a greater risk of fatigue failure. The safety factor of the two-layer structure (33.44) is significantly superior to that of the three-layer structure (15.33), demonstrating distinct advantages in fatigue design.

(2) Axial Elongation Analysis

Figure 6b shows the axial displacement contours of the two actuator configurations under the same operating condition. The maximum axial displacement of the two-layer bellows actuator is $U_{max2} = 1.428$ mm, whereas that of the three-layer bellows actuator is $U_{max3} = 1.080$ mm. The displacement of the two-layer structure is therefore approximately 32.2% greater than that of the three-layer configuration.

Based on Equation (15), the displacement-stress efficiency indices for both structural configurations are calculated as follows:

For the two-layer bellows structure,

$$\eta_2 = \frac{1.428}{0.08971} \approx 15.9$$

For the three-layer bellows structure,

$$\eta_3 = \frac{1.080}{0.1957} \approx 5.52$$

The comprehensive efficiency of the two-layer structure is 2.88 times that of the three-layer structure. Integrating the three evaluation metrics of strength, elongation, and efficiency, it is evident that the two-layer bellows structure exhibits lower stress, greater displacement, and superior comprehensive efficiency under identical gas pressure, demonstrating distinct overall advantages. This indicates that the two-layer structure can achieve greater effective axial deformation with lower stress under identical pressure conditions, exhibiting superior strength-deformation characteristics. It serves as an important parametric basis for more efficient and durable long-cycle driving scenarios in wall-climbing robots. The displacement-stress efficiency index η is introduced to evaluate the comprehensive driving capability of both structures, with this comprehensive evaluation methodology consistent with the modeling and analysis framework for multi-degree-of-freedom pneumatic bending artificial muscles [20]. The advantages of the bidirectional driving structure of bellows in axial output efficiency have also been validated in similar research [21,22]. Consequently, the subsequent prototype design and experimental verification both employ the two-layer bellows structure actuator as the research subject.

3.1.2. Investigation of Driving Characteristics with Different Lengths

The geometric dimensions of soft pneumatic actuators have a decisive influence on their bending capability, strain energy consumption, and structural rigidity, with significant mutual constraints existing among these three factors [23]. For specific application scenarios such as wall-climbing robots, excessive pursuit of a single performance index often results in insufficient system rigidity or increased control difficulty. Therefore, evaluating the influence of different lengths on actuator performance and identifying an optimal length range that achieves the best balance between motion output and control linearity is critical for achieving reliable multi-degree-of-freedom motion decoupling.

To systematically evaluate the effect of actuator effective length on bending and elongation characteristics, this study selected three typical length values—10 mm, 20 mm, and 40 mm for comparative investigation. This sampling approach, which maintains a 2-fold ratio relationship between adjacent intervals, can effectively capture the non-monotonic characteristics of the performance-length curve with minimal simulation and experimental costs.

The candidate lengths (10, 20, 40 mm) were constrained by the geometry of the end cap and air-distribution manifold (Table 1): lengths below 10 mm leave insufficient bonding area between the bellows and end cap, while lengths above 40 mm exceed the effective stroke range compatible with the manifold's fixed air-channel routing.

Table 1. Geometric and structural parameters of the proposed soft actuator.

Parameter Description	Symbol	Value (mm)
Overall length	L	60
Width of the upper air-guide plate	H	40
Height of the upper air-guide plate	b	7
Width of the lower air-guide plate	h	35
Height of the lower air-guide plate	c	5
Length of the end effector	a	25
Height of the end effector	e	20
Outer diameter of the upper-layer soft actuator	R_1	4
Inner diameter of the upper-layer soft actuator	r_1	3
Outer diameter of the lower-layer soft actuator	R_2	6
Inner diameter of the lower-layer soft actuator	r_2	5
Pneumatic channel diameter	d	2

To ensure consistency between experimental and simulation boundary conditions, the radial degrees of freedom of the actuator outer wall were appropriately constrained in the simulation to equivalent the limiting effect of flexible fine wires in experiments. Referencing the parametric analysis methods for structural optimization of existing pneumatic soft actuators, the effects of the length variable on driving performance were effectively evaluated.

(1) Bending Angle Analysis

Finite element simulation analysis was conducted on the bending angle and axial elongation of soft actuators at different lengths. Figure 7 presents the bending angle variation curves for actuators with lengths of 10 mm, 20 mm, and 40 mm as single-chamber input gas pressure varies from 0 to 0.04 MPa.

Figure 7 presents the simulated curves of bending angle variation with gas pressure for three soft actuators with lengths of 10 mm, 20 mm, and 40 mm. Overall, all three bending angle curves increase monotonically with increasing gas pressure. Among these, the 10 mm actuator exhibits the largest bending angle at each pressure point and demonstrates the fastest rate of increase with rising pressure; the 20 mm actuator shows intermediate bending angles with relatively uniform stepwise growth and no obvious sudden changes; and the 40 mm actuator exhibits the smallest bending angle at low pressure but demonstrates a distinct jump in the intermediate pressure range, after which the rate of increase slows down, exhibiting pronounced nonlinear characteristics.

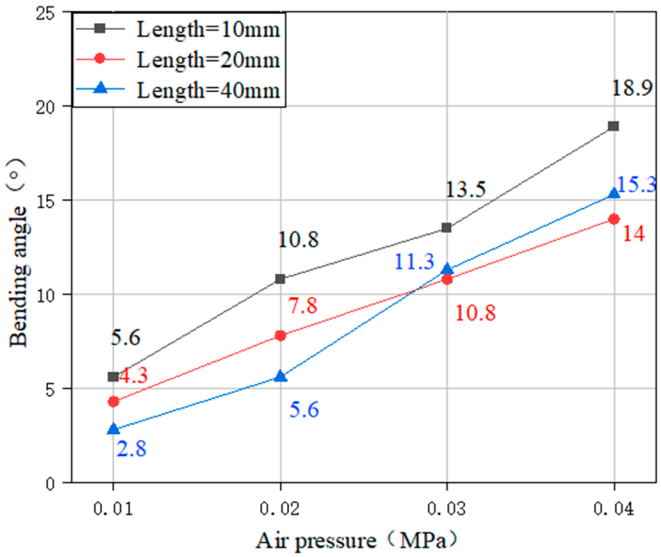


Figure 7. Simulation results of bending angle vs. input air pressure at 10, 20, and 40 mm actuator lengths.

(2) Axial Elongation Analysis

Figure 8 presents the simulated curves of axial elongation variation with gas pressure for the same three actuators of different lengths. All three groups of axial elongation increase with rising gas pressure, with larger lengths resulting in greater absolute elongation values: the 40 mm group exhibits the largest elongation, followed by the 20 mm group, and the 10 mm group shows the smallest. All three curves demonstrate approximately linear growth, with the 40 mm group showing a slightly accelerated rate of increase at high pressure, while the 20 mm and 10 mm groups exhibit relatively stable growth slopes with no obvious nonlinear discontinuities.

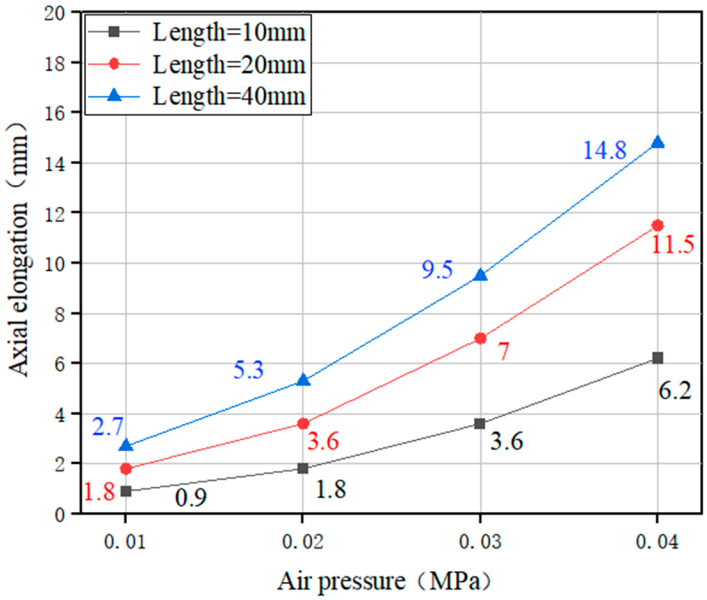


Figure 8. Simulation results of axial elongation vs. input air pressure at 10, 20, and 40 mm actuator lengths.

From the two performance indicators of bending angle and axial elongation, the 10 mm actuator, although exhibiting large bending angles, demonstrates the smallest axial deformation, resulting in limited end-effector workspace that is difficult to simulate the

realistic swing amplitude of actual legs and fails to meet the joint deformation requirements of wall-climbing robots during obstacle crossing or wall transitions. Additionally, the relatively high stiffness of the short structure air chamber leads to more pronounced local stress concentration under long-term pneumatic cycling, readily inducing fatigue failure. Although the 40 mm actuator possesses the strongest deformation capability, its bending response exhibits obvious nonlinear jumps in the intermediate pressure range, and its axial elongation rate accelerates at high pressure, indicating that its excessive aspect ratio leads to decreased structural stability and response predictability. The excessive air chamber volume results in prolonged fill-discharge response times under identical pressure, not only slowing joint motion frequency but also introducing additional volume and inertia that are detrimental to the compact arrangement and energy efficiency of multi-joint wall-climbing robots, and incompatible with robot kinematics modeling and precise control.

In contrast, for wall-climbing robot applications, the 20 mm actuator demonstrates good response linearity on both bending angle and axial elongation indicators, with smooth growth processes and no obvious discontinuities. Simultaneously, its absolute deformation values are sufficient to meet the joint range of motion required for wall-climbing robot gait design and wall transitions. Therefore, the 20 mm actuator was selected not because it provided the maximum deformation output, but because it achieved a better balance among deformation capability, response linearity, structural stability, and control predictability, which are critical requirements for wall-climbing robot joints. Accordingly, this study selected 20 mm as the structural length of the soft joint for wall-climbing robots.

We acknowledge that, in principle, a pressure-to-output mapping (e.g., a calibrated look-up table or a fitted nonlinear function) could be established to compensate for the nonlinear response of the 10 mm or 40 mm actuators, allowing accurate control even without linearity. However, we favor the 20 mm configuration for three practical reasons that go beyond linearity alone. First, the 40 mm actuator's nonlinearity arises from a sudden jump in the mid-pressure range (Section 3.1.2) rather than a smooth, monotonic nonlinear curve; such jumps are difficult to calibrate reliably because the mapping is highly sensitive to small variations in manufacturing tolerance and material batch, meaning a look-up table calibrated on one prototype may not transfer accurately to another. Second, an accurate nonlinear mapping requires dense calibration data across the full pressure range for every fabricated unit, which is impractical for a wall-climbing robot intended for batch production and field deployment. Third, near the nonlinear jump region, the actuator's response also exhibits increased hysteresis between pressurization and depressurization (Section 4.4), which a static pressure-to-output mapping cannot fully capture, introducing additional control error beyond what calibration alone can correct. The 20 mm configuration avoids these practical difficulties by providing a response that is both accurate and robust to manufacturing variation without requiring per-unit calibration, in addition to satisfying the task-driven elongation and bending-angle requirements discussed above.

3.2. Effect of Material Hardness on Driving Characteristics

3.2.1. Bending Angle Analysis

Figure 9 presents the bending characteristics variation patterns of pneumatic bellows actuators fabricated from silicone materials with different hardness levels under single-chamber inputs at varying gas pressures.

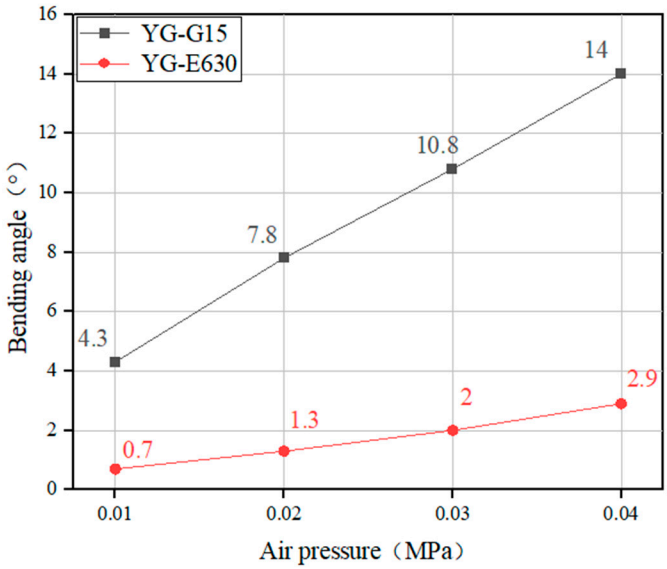


Figure 9. Effect of hardness on bending angle.

From the analysis of Figure 9, within the gas pressure range of 0.01–0.04 MPa, the bending angles of actuators fabricated from both materials increase with rising input gas pressure, but the growth rates differ significantly. Under identical pressure conditions, the bending angle of the YG-G15 actuator is markedly larger than that of YG-E630. The fundamental reason lies in the different hyperelastic constitutive characteristics of the two materials: YG-G15 has Yeoh model parameters C_{10} = 0.0397 MPa and C_{20} = 0.0092 MPa with lower elastic modulus, capable of generating greater radial expansion deformation under identical internal pressure, thereby producing larger driving torque; YG-E630 has C_{10} = 0.1937 MPa and C_{20} = 0.0466 MPa with higher elastic modulus, exerting stronger constraint on air chamber expansion, resulting in suppressed bending output. As gas pressure increases, the bending angle discrepancy between the two materials further widens, indicating that material hardness exerts significant influence on the driving performance of the actuator [24,25].

3.2.2. Axial Elongation Analysis

Figure 10 presents the axial elongation variation patterns of the 20 mm actuator under different material hardness conditions. As input gas pressure increases from 0.01 MPa to 0.04 MPa, the axial elongation of both materials exhibits an upward trend, but the growth rates show obvious differences. The low-hardness material YG-G15 produces greater axial deformation under identical gas pressure, while the high-hardness material YG-E630, due to its higher elastic modulus, exerts stronger constraint on air chamber expansion, resulting in lower elongation output. This finding is consistent with the conclusions from the bending angle analysis, further validating that YG-G15 is the optimal material selection for actuator fabrication in this study.

3.3. Optimal Selection of Actuator Structural Parameters

Based on theoretical calculations and simulation analysis, the optimal structural parameters of the soft actuator were determined. As shown in Figure 11, the two-layer soft actuator comprises three bellows pneumatic actuators and upper, middle, and lower triangular end plates. The actuator is fabricated from elastic silicone material and undergoes axial elongation and bending deformation under radial constraint after pressurization. The specific structural parameters are detailed in Table 1.

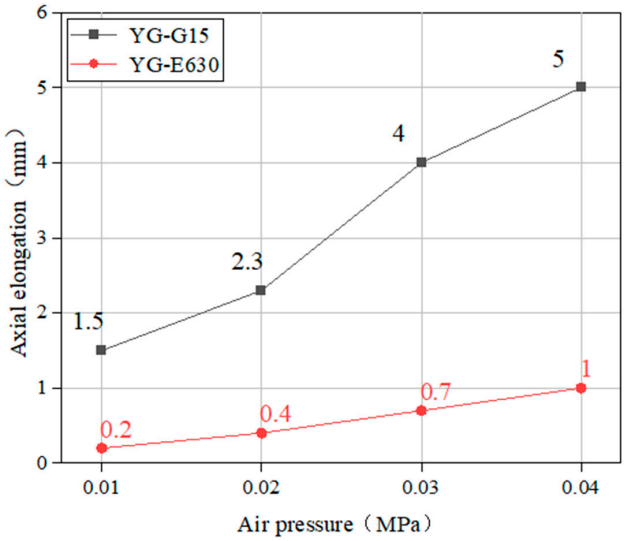
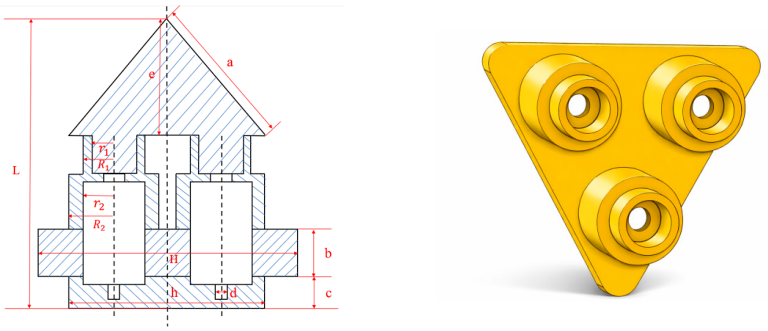


Figure 10. Effect of hardness on axial elongation.



(**a**) (**b**)

Figure 11. Structure of the soft actuator. (**a**) Internal structure of the soft actuator. (**b**) External view of the soft actuator.

Through finite element simulation, the optimal structural configuration of the actuator was determined across three dimensions: bellows layer number, length, and material hardness—specifically, a two-layer bellows structure, 20 mm effective length, and low-hardness YG-G15 material. Simulation results demonstrate that this configuration achieves optimal balance among strength safety, driving efficiency, and response linearity. However, the simulation itself is still based on idealized assumptions and simplified boundary conditions; therefore, whether its predictions accurately reflect the actuator's driving characteristics under actual working conditions requires validation through physical-prototype experiments. In particular, the finite element evaluations in Section 3.1 were conducted under internal pneumatic loading only; no external boundary conditions representative of wall-attachment operation—such as gravitational loading, contact/reaction forces from the climbing surface, or payload from onboard components—were included. The reported safety factor and displacement-stress efficiency therefore characterize the actuator's intrinsic pneumatic actuation performance rather than its structural reliability under actual climbing conditions, where structural rigidity and wall-conformity compliance generally present a design trade-off. To this end, the following section will fabricate physical prototypes based on the aforementioned optimization parameters, establish a pneumatic experimental platform, and conduct systematic experimental testing of axial elongation and bending angle characteristics to verify the engineering validity of the theoretical model and simulation results.

4. Prototype Fabrication and Experimental Verification

4.1. Actuator Prototype Fabrication and Experimental Platform Establishment

4.1.1. Actuator Prototype Fabrication

Based on the above simulation results, the optimal actuator configuration was determined to consist of a two-layer bellows structure with an effective length of 20 mm. The actuator was fabricated using YG-G15 two-part silicone rubber with a Shore hardness of 15. A molding-based fabrication process was adopted, and the detailed manufacturing procedure is illustrated in Figure 12. The fabrication process mainly consists of the following steps:

(1) Mold Preparation: The outer bellows mold and the inner core mold were fabricated according to the optimized design parameters. PLA was selected as the mold material, and all mold components were manufactured using three-dimensional (3D) printing technology.

(2) Silicone Preparation: Components A and B of the YG-G15 two-part silicone rubber were weighed at a mass ratio of 1:1 and thoroughly mixed using a mechanical stirrer for 3 min. The mixture was then allowed to stand for 2 min to remove entrapped air bubbles introduced during mixing, thereby preventing pore defects after curing and ensuring the airtightness of the actuator.

(3) Casting and Curing: The prepared silicone mixture was slowly poured into the outer mold, after which the inner core mold was centrally positioned and fixed to ensure a uniform wall thickness throughout the bellows structure. After casting, the assembly was cured at room temperature (25 °C) for 4 h.

(4) Demolding and Post-Processing: After complete curing, the inner core mold was removed first, followed by careful removal of the outer mold. The bellows surface was then inspected for potential defects. Subsequently, the pneumatic tubing interfaces were trimmed, and the upper end cap and end effector were bonded to the bellows structure to complete the actuator assembly.

(5) Airtightness Verification: The assembled actuator was connected to the pneumatic supply system and pressurized to 0.01 MPa for 30 s. Subsequent experiments were conducted only after confirming the absence of any detectable air leakage.

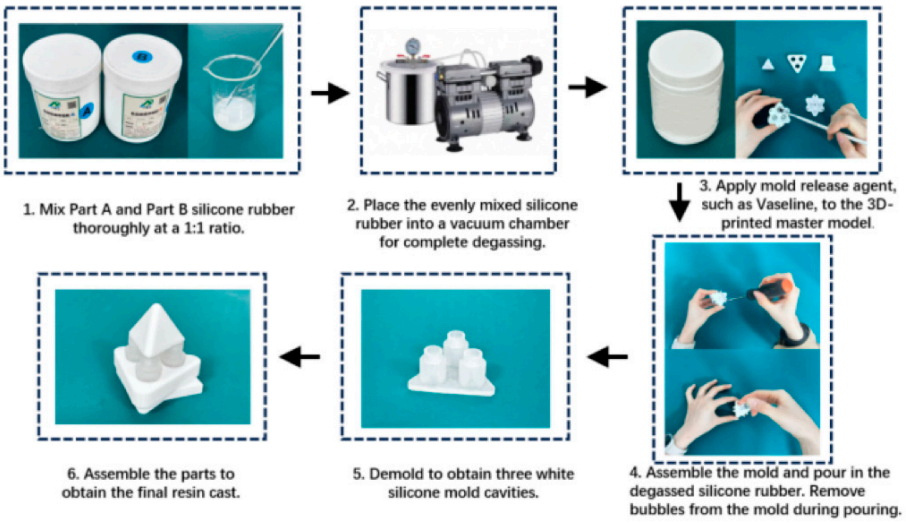


Figure 12. Making steps of the actuator.

The three chambers (R_1, R_2, R_3) of the three-chamber bellows soft actuator are uniformly distributed along the circumferential direction, with an angular spacing of 120°

between the centerlines of adjacent chambers. Depending on the pressurization combinations of the three chambers, the actuator exhibits a total of $2^3 = 8$ fundamental motion states, as illustrated in Figure 13. These states span the complete motion space of the actuator, ranging from a fully stationary configuration to omnidirectional bending motions.

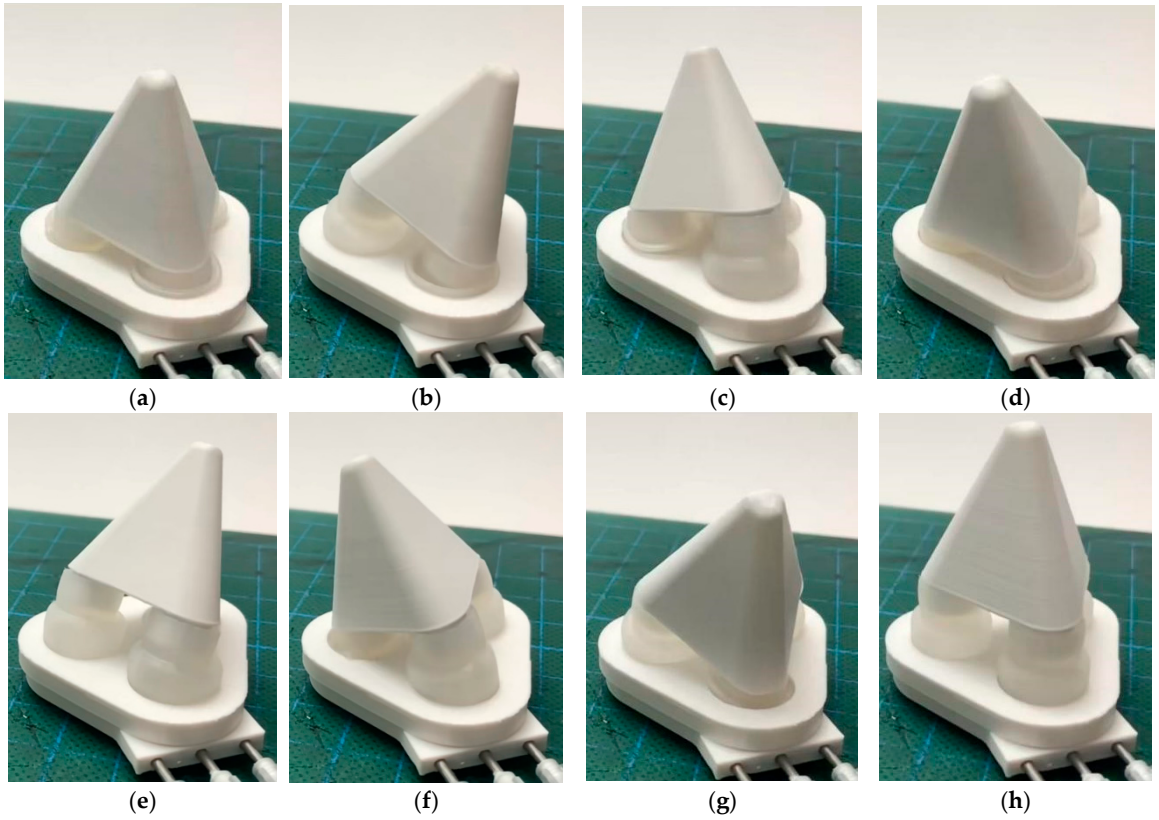
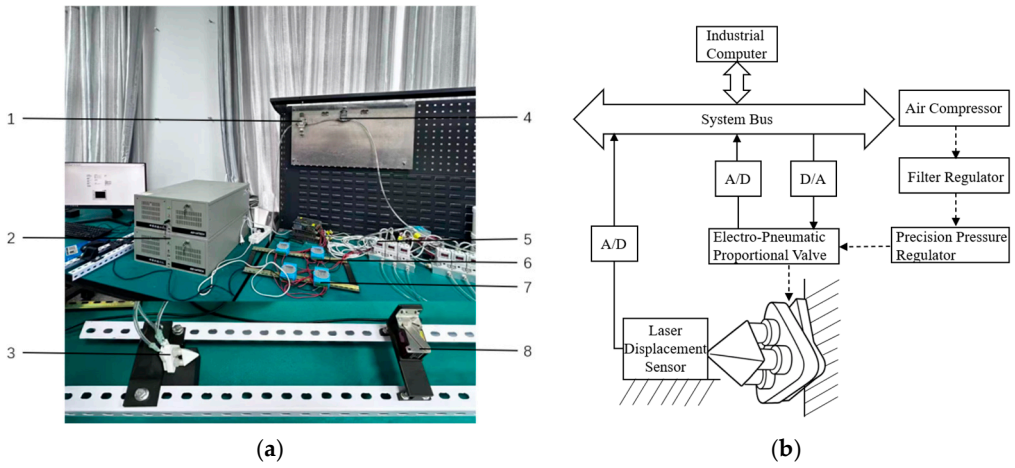


Figure 13. Schematic illustration of the eight basic motion states of the soft actuator. (**a**) Near axial stretch. (**b**) Right bending. (**c**) Backward bending. (**d**) Left bending. (**e**) Front-right bending. (**f**) Rear-left bending. (**g**) Forward bending. (**h**) Near axial extension.

4.1.2. Experimental Setup of the Pneumatic Control Platform

To investigate the actuation characteristics of the proposed three-degree-of-freedom pneumatic artificial muscle actuator, an experimental platform was established, as shown in Figure 14. The operating principle of the platform is as follows. An air compressor serves as the pneumatic power source and supplies compressed air to the system. The compressed air first passes through an air treatment unit for filtration and pressure regulation, and is subsequently delivered to an electro-pneumatic proportional valve for precise pressure control. The regulated air pressure is then applied to the soft actuator to generate the desired motion, while the operating parameters of the actuator are monitored in real time using sensors. The main specifications of the experimental platform are summarized in Table 2.

To improve motion stability during the experiments, appropriate flexible constraints were applied to the outer wall of the actuator. This treatment effectively reduced radial asymmetric deformation and minimized its influence on the measurement results, thereby improving the repeatability and accuracy of the experimental data.



(**a**) (**b**)

Figure 14. Experimental platform for a pneumatic soft bellows actuator and the schematic diagram. (**a**) Experimental setup. (**b**) Operating principle: 1. Filter regulator. 2. Host computer. 3. Soft actuator. 4. Precision pressure regulating valve. 5. Electro-pneumatic proportional valve. 6. AO module. 7. AI module. 8. Laser displacement sensor.

Table 2. Components of the pneumatic experimental platform.

Component	Model	Specification
Air compressor	ZP2-1280	Rated discharge pressure: 0.8 MPa; air tank capacity: 8 L
Filter regulator	AW20-02B	Pressure regulation range: 0.05–0.85 MPa; filtration accuracy: 5 μm
Electro-pneumatic proportional valve	TTV1010-041S	Pressure regulation range: 0.005–0.1 MPa; linearity: within 1% F.S.
Force sensor	DJSX-16-2KG	Measurement range: 0–20 N; hysteresis: 0.1% F.S.; nonlinearity: 0.1% F.S.
Signal transmitter	DJYB-800A	Supply voltage: 18–30 V; frequency: 50/60 Hz; measurement error: 0.1% F.S.
PCI data acquisition card	PCI-1721-BE	PCI data acquisition card
Industrial computer	IPC610-L	Core i7-6700,3.4 GHz/64 GB

For the axial elongation tests, all three chambers were pressurized equally ($p_1 = p_2 = p_3 = p$) from 0 to 0.04 MPa in 0.01 MPa increments; elongation was measured via laser displacement sensor. For the bending tests, chamber R_1 alone was pressurized over the same range while R_2, R_3 were held at 0 MPa (corresponding to $\varphi = 0°$); bending angle was measured from calibrated side-view images. Each configuration (10/20/40 mm × two-layer/three-layer × YG-G15/YG-E630) was fabricated and tested as an independent physical prototype.

4.2. Experimental and Simulation Comparative Analysis of Axial Elongation Characteristics

Throughout Section 4, "FE Simulation" refers specifically to the finite element (Abaqus) results of Section 3.

4.2.1. Axial Elongation Experimental Analysis

The axial elongation of the actuator characterizes the extension induced by the resultant axial force generated by the three pneumatic chambers. When identical pressure is applied to all chambers ($p_1 = p_2 = p_3 = p$), the bending moments produced by the chambers are mutually balanced, resulting in pure axial extension without any bending deformation.

In this case, the actuator elongation is primarily determined by the average chamber pressure, and the corresponding theoretical model is given by

$$\Delta L = \alpha \frac{p_1 + p_2 + p_3}{3} L_0 \tag{16}$$

where

L_0 denotes the natural (initial) length of the actuator;
α is the axial compliance coefficient.

To simplify the theoretical axial elongation model given in Equation (4), a lumped parameter is introduced and defined as:

$$\alpha = \frac{\pi D_2^2}{4\pi G_R \left(D_1^2 - D_2^2\right)} - \frac{\pi\left(D_1^2 - 2D_2^2\right)}{L_0} \tag{17}$$

According to Equation (16), the axial elongation is proportional to the average pressure of the three chambers and is decoupled from both the bending direction and bending angle. Therefore, independent regulation of these three motion parameters can theoretically be achieved.

4.2.2. Experimental and Simulation Comparative Analysis of Actuator Axial Elongation Under Different Lengths

Figure 15 is the comparative analysis of axial elongation between experiment and simulation for the 10 mm actuator.

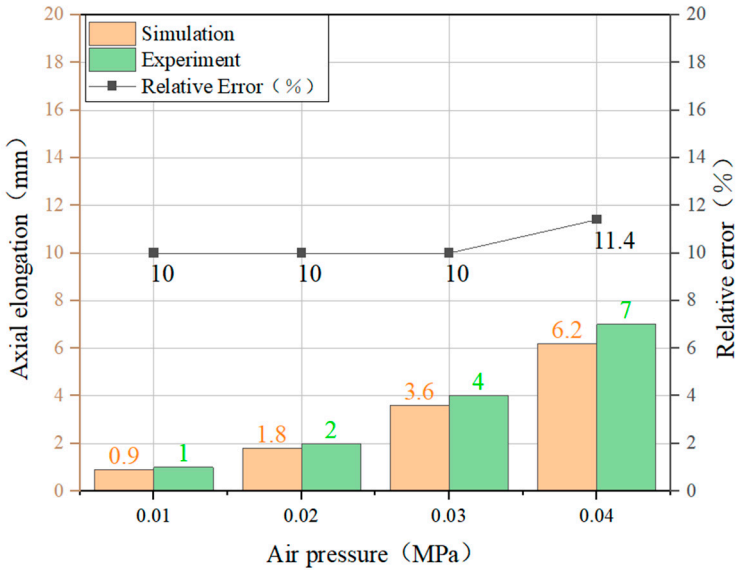


Figure 15. Simulation and experimental comparison of axial elongation variation with input air pressure at 10 mm actuator length.

Figure 16 is the comparative analysis of axial elongation between experiment and simulation for the 20 mm actuator.

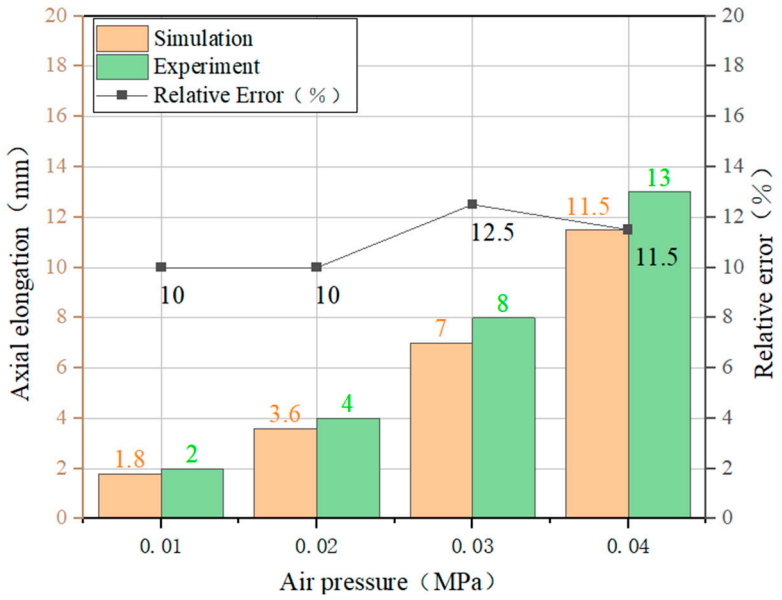


Figure 16. Simulation and experimental comparison of axial elongation variation with input air pressure at 20 mm actuator length.

Figure 17 is the comparative analysis of axial elongation between experiment and simulation for the 40 mm actuator.

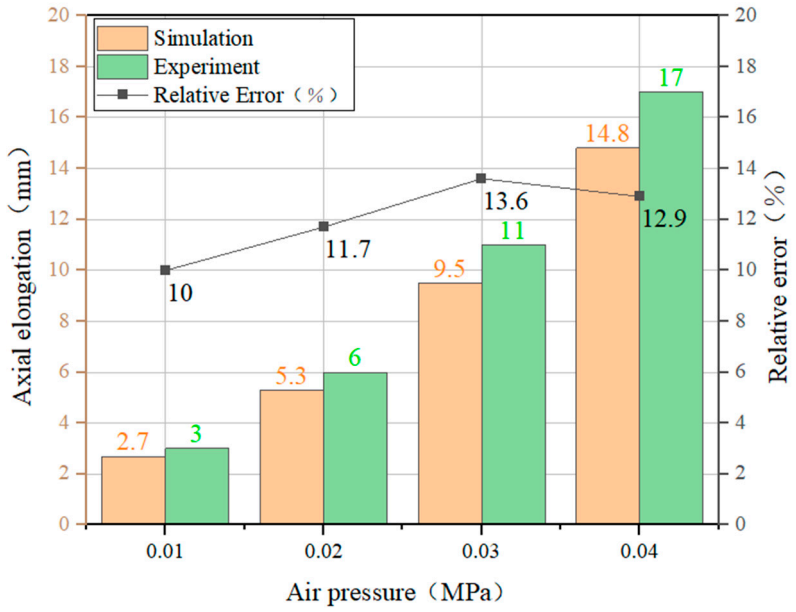


Figure 17. Simulation and experimental comparison of axial elongation variation with input air pressure at 40 mm actuator length.

From the simulation-experiment relative error results of axial elongation, the relative errors of all three actuators with different lengths fall within the reasonable range of 10–14%, with errors showing a slight upward trend as actuator length increases: the average values are approximately 10.4% for 10 mm, 11.0% for 20 mm, and 12.1% for 40 mm. This indicates that as the aspect ratio increases, the influence of material nonlinear effects on simulation accuracy gradually strengthens. Considering both deformation capability and simulation-experiment consistency, the 20 mm actuator maintains a lower error level superior to the 40 mm configuration while possessing greater axial deformation margin

superior to the 10 mm design, making it a compromise solution that balances both accuracy and deformation capability.

As shown in Figure 18, the axial elongation of all three actuators with different lengths increases monotonically with rising gas pressure, with longer lengths producing greater elongation: the 40 mm actuator reaches experimental elongation of 17 mm at 0.04 MPa, compared to a simulated value of 14.8 mm; the 20 mm actuator exhibits experimental elongation of 13 mm versus a simulated value of 11.5 mm; the 10 mm actuator demonstrates experimental elongation of 7 mm compared to a simulated value of 6.2 mm. The experimental values at each length are slightly higher than the simulated values, primarily due to the viscoelastic effects of the actual silicone material and deviation of assembly preload forces from the ideal simulation boundary conditions; however, the overall errors remain within a relatively small range, validating the correctness of the axial elongation analytical model and confirming the approximate proportional relationship between elongation and actuator length.

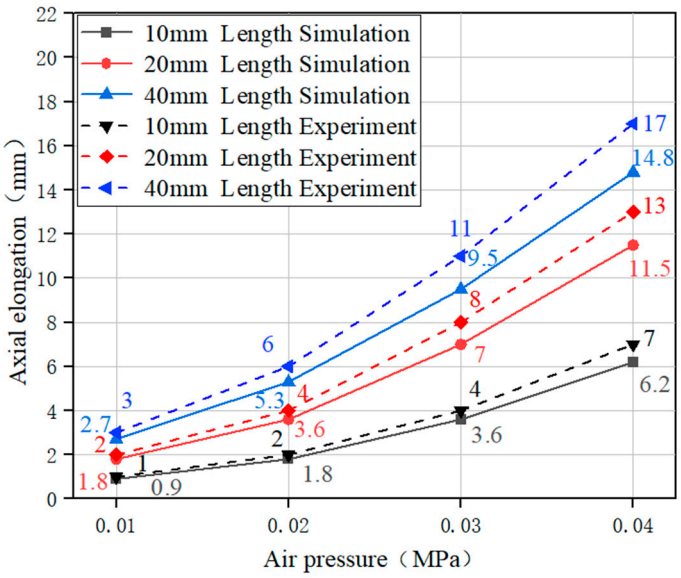


Figure 18. Comparison of simulation and experimental results of axial elongation vs. input air pressure at 10, 20, and 40 mm actuator lengths.

4.2.3. Back-Calibration and Applicability Range of the Analytical Linear Model

While Section 4.2.2 validated the finite element simulation against experimental data, the simplified analytical model of Equation (16) which assumes a constant axial compliance coefficient α had not been independently verified against experimental measurements. To assess its applicability, α was back-calculated from the four experimental data points of the 20 mm actuator using $\alpha = \Delta L/(p \cdot L_0)$.

The results show that α remains highly stable ($\alpha \approx 10.0$) in the low-pressure range of 0.01–0.02 MPa, but increases markedly at 0.03 and 0.04 MPa. Using the low-pressure-calibrated value ($\alpha = 10$) to predict elongation at higher pressures yields theoretical values of 6.0 mm and 8.0 mm at 0.03 MPa and 0.04 MPa, respectively, corresponding to relative errors of 25% and 38.5% against the experimental values (8.0 mm and 13.0 mm).

These results indicate that the linear model of Equation (16) provides an accurate first-order approximation of actuator behavior only within the low-pressure, small-strain regime (approximately 0.01–0.02 MPa). As pressure increases to 0.03–0.04 MPa, the strain-softening behavior of the hyperelastic silicone material and the geometric nonlinearity associated with bellows wall thinning become increasingly significant, causing the constant-α assumption to break down. This finding is consistent with the material nonlinearity discussion in

Section 4.2.2 and confirms that a single global compliance coefficient is insufficient to describe the actuator's full-range pressure–elongation response.

Accordingly, α is recommended to be identified by linear regression on low-pressure experimental data (as in Table 3) rather than derived purely analytically from Equation (17) under the linear-elastic assumption of Equation (5), since the latter does not account for hyperelastic strain softening and consequently produces substantially larger deviations when extrapolated to higher working pressures.

Table 3. Back-calculated axial compliance coefficient α at different pressures (20 mm actuator).

Pressure P (MPa)	Experimental ΔL (mm)	Back-Calculated α
0.01	2.0	10.0
0.02	4.0	10.0
0.03	8.0	13.3
0.04	13.0	16.25

It should be emphasized that the back-calibration analysis above, together with the length- and bending-angle comparisons in Sections 4.2.2 and 4.3, validates the model only under two boundary parameter configurations: equal three-chamber pressure ($p_1 = p_2 = p_3$, pure elongation) and single-chamber pressurization ($p_2 = p_3 = 0$, pure bending at $\varphi = 0°$). These two configurations validate Equations (4), (8) and (14) individually, but do not constitute direct experimental verification of the decoupled model's central claim—namely, that elongation and bending remain mutually independent under simultaneous, unequal multi-chamber pressure inputs ($p_1 \neq p_2 \neq p_3$). Under the small-deformation assumptions underlying the present derivation, the combined-input response is expected to correspond to the linear superposition of the two individually validated responses; the results above provide indirect support for this assumption but do not quantify any nonlinear interaction between the two motion channels under combined actuation. Direct experimental validation under simultaneous, non-equal three-chamber pressure combinations—with measured ΔL, φ, and θ compared against Equations (4), (8) and (14), respectively—was not performed in this study and is addressed as future work in Section 5.1.

4.3. Experimental and Simulation Comparative Analysis of Bending Deformation Characteristics

For the single-chamber bending tests reported in this section, chamber R_1 alone was pressurized over 0.01–0.04 MPa while R_2 and R_3 were held at atmospheric pressure (0 MPa gauge). By the symmetry established in Section 2.3, this corresponds to bending direction $\varphi = 0°$ (the boundary case $0 \leq \varphi \leq \frac{\pi}{6}$ in Figure 4 Region I). The bending angle θ reported is the angle between the actuator's undeformed central axis and the line connecting the base center to the tip center, measured in the plane containing both the undeformed axis and $\varphi = 0°$, from calibrated side-view images.

Experimental and Simulation Comparative Analysis of the Bending Angle of Actuators with Different Lengths

Figure 19 is the comparative analysis of bending angle between experiment and simulation for the 10 mm actuator.

Figure 20 is the comparative analysis of bending angle between experiment and simulation for the 20 mm actuator.

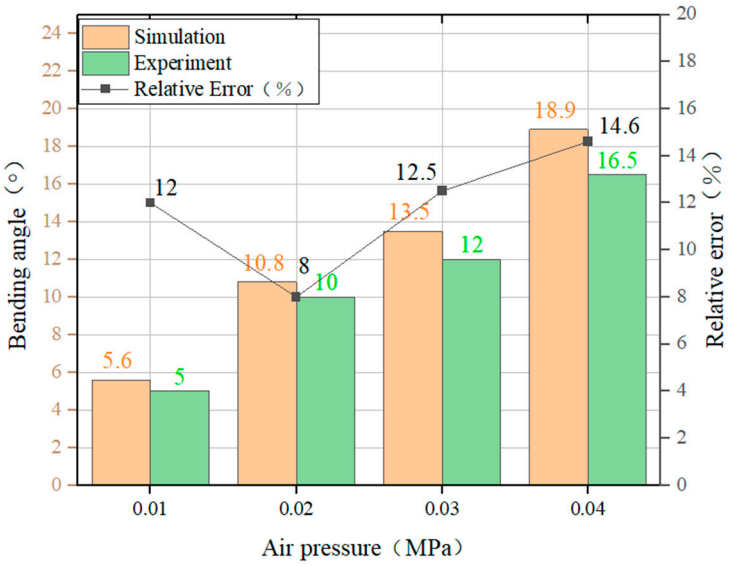


Figure 19. Simulation and experimental comparison of bending angle variation with input air pressure at 10 mm actuator length.

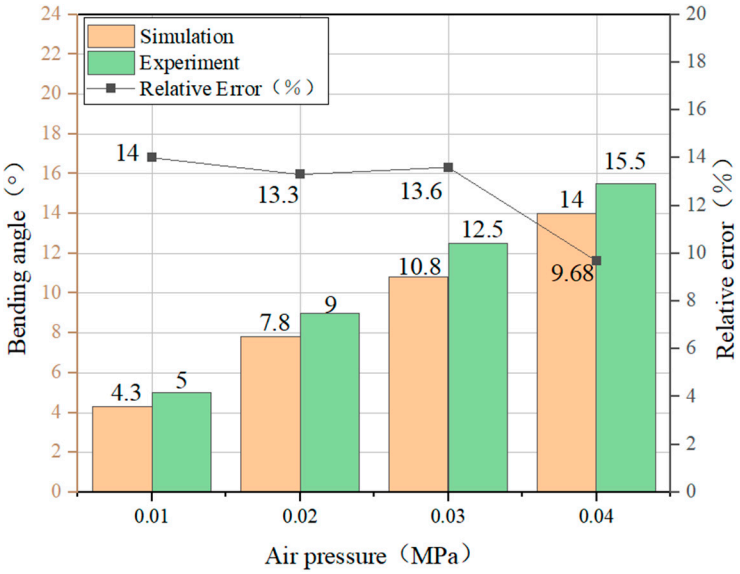


Figure 20. Simulation and experimental comparison of bending angle variation with input air pressure at 20 mm actuator length.

Figure 21 is the comparative analysis of bending angle between experiment and simulation for the 40 mm actuator.

Comparative analysis of simulation-experiment data on bending angles for the three actuators with lengths of 10 mm, 20 mm, and 40 mm reveals average relative errors ranging from 11.8% to 12.6%, with no significant differences among the three groups. However, examining the trend of error variation with pressure changes, the 10 mm group shows increasing rather than decreasing relative errors as actual working pressure is approached, indicating diminished prediction capability of its simulation model in the high-pressure range; whereas the 20 mm group demonstrates distinct convergence of relative errors in this pressure range, indicating superior simulation-experiment consistency at actual working pressures and more reliable model prediction of real response, which is more conducive to subsequent control implementation based on the simulation model. Considering compre-

hensive deformation capability, structural rigidity, and model reliability within the working pressure range, this study selected 20 mm as the structural parameter for the soft joint.

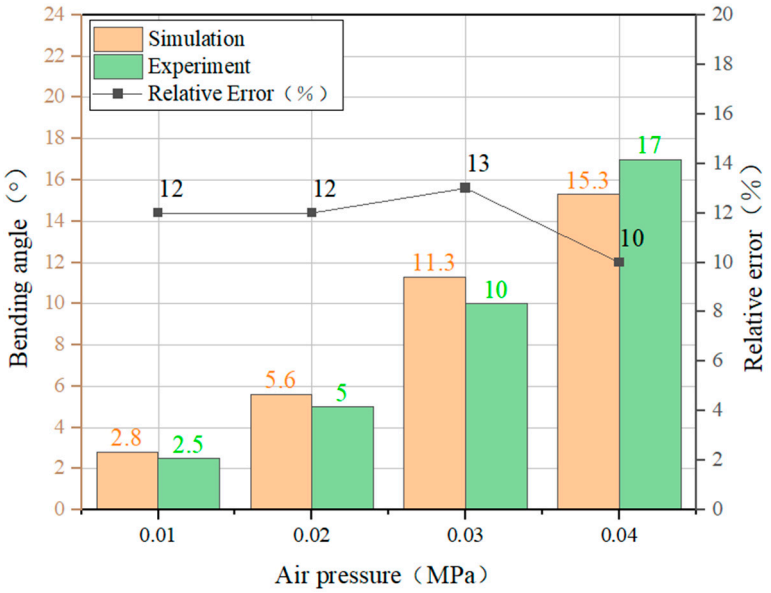


Figure 21. Simulation and experimental comparison of bending angle variation with input air pressure at 40 mm actuator length.

From Figure 22, the comparative results of simulation and experiment for bending angle variation with gas pressure of the three actuators with different lengths are shown. Unlike axial elongation, bending angle does not vary monotonically with length: the 10 mm actuator exhibits the largest bending angle across the entire pressure range among the three; the 20 mm actuator shows the smallest bending angle; the 40 mm actuator demonstrates intermediate bending angles at low pressure, but the rate of increase accelerates significantly with rising pressure, reaching an experimental value of 17° at 0.04 MPa, surpassing the other two. All three lengths demonstrate good agreement between simulation and experimental results with maximum relative errors controlled within reasonable ranges, validating that the bending angle analytical model possesses good applicability for actuators of different lengths. This also indicates that bending angle is the result of the coupled action of two effects—end moment arm and structural relative rigidity—rather than a simple monotonic function of length.

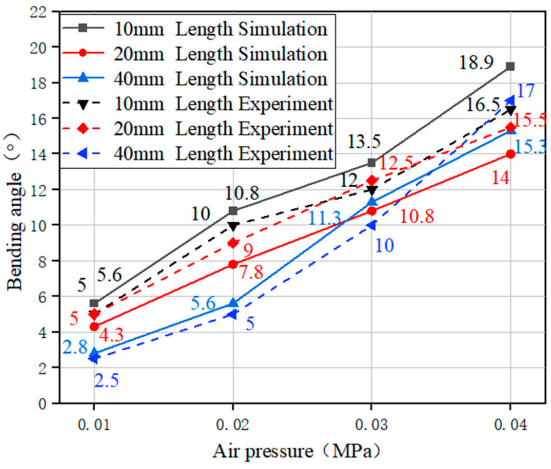


Figure 22. Comparison of simulation and experimental results of bending angle vs. input air pressure at 10, 20, and 40 mm actuator lengths.

4.4. Error Analysis

From the root mean square error (RMSE) statistical results in Table 4, the RMSE of axial elongation exhibits a decreasing-then-increasing trend, while the RMSE of bending angle shows an overall increasing fluctuation trend, with both reaching maximum values at the highest working pressure. These results indicate that the simulation model of the soft actuator can predict its mechanical response relatively accurately at low pressure ranges; however, as pressure increases and material deformation magnitude grows, the discrepancy between simulation and experiment expands significantly. Further combined with relative error analysis, At the optimal configuration, the maximum relative errors are 12.5% for axial elongation and 14% for bending angle, suggesting that the model effectively reproduces the actuator's actual motion performance. Nevertheless, certain discrepancies still exist between the theoretical model and experimental results, with the primary reasons as follows:

(1) Modeling error arising from constant-curvature assumption. To reduce model complexity, this study employed the constant-curvature assumption to establish the actuator kinematics model, assuming the actuator maintains constant curvature throughout the entire bending process. In reality, due to non-uniform axial rigidity distribution of the bellows structure, the local expansion extent of each air chamber differs after pressurization. Particularly under higher input pressures, the actuator experiences localized non-uniform deformation, causing actual curvature to vary along the axis. Consequently, certain errors are inevitably generated between the theoretical model and actual deformation, representing one of the primary sources of error in this study.

(2) Error from material nonlinearity. The theoretical model employs equivalent elastic parameters to describe the mechanical properties of silicone material, whereas actual YG-G15 silicone is a typical hyperelastic material with obviously nonlinear stress-strain relationships. Additionally, silicone exhibits Mullins effects and viscoelastic characteristics during repeated pressurization–depressurization cycles, causing material stiffness to vary with deformation history. Since these factors were not adequately considered in the theoretical model, discrepancies exist between theoretical calculations and experimental results.

(3) Manufacturing tolerance error. The actuator is fabricated using silicone casting molding processes. Inevitable problems during actual manufacturing include non-uniform wall thickness, bellows dimension errors, deviations in air chamber center positions, and mold assembly errors. These manufacturing tolerances cause differences in force distribution among the three chambers compared to the theoretical model, thereby affecting the actual bending angle and axial elongation of the actuator.

(4) Gas pressure control error. Although a pressure regulator was employed to control input pressure during experiments, discrepancies still exist between the actual gas pressure inside the actuator and the set value due to gas source fluctuation, pressure loss in tubing, and electromagnetic valve response hysteresis. Particularly at low-pressure conditions, slight pressure fluctuations can significantly affect experimental results.

(5) Measurement error. This study obtained actuator bending angle and axial elongation through image measurement. During experimentation, camera calibration error, image resolution, characteristic point extraction accuracy, and manual reading errors all affect final measurement results. Additionally, the actuator exhibits slight spatial deflection under pressure, while two-dimensional visual measurement only captures the projection outline of the actuator. Slight spatial deflection of the actuator introduces projection error, affecting the measurement precision of bending angle and axial elongation.

Table 4. Root mean square error (RMSE) statistics.

	Gas Pressure Value P/MPa	0.01	0.02	0.03	0.04
Axial Elongation	RMSE Experiment-Simulation	0.796	0.480	1.066	1.605
Bending Angle	RMSE Experiment-Simulation	0.560	0.902	0.843	1.798

In conclusion, errors between the theoretical model and experimental results primarily originate from the constant-curvature assumption, material nonlinearity, manufacturing tolerance, and experimental measurement errors. Among these, the constant-curvature assumption and material nonlinearity are the primary sources of error. Nevertheless, the model's prediction errors for actuator axial elongation and bending angle remain within 15%, indicating that the established theoretical model can relatively accurately describe actuator motion characteristics and provide theoretical basis for actuator structural design, parameter optimization, and motion control. Subsequent research will further incorporate hyperelastic constitutive models and non-constant-curvature modeling methods to improve model prediction accuracy under large-deformation conditions.

Through systematic experimental testing of bending angle and axial elongation for actuators with three different lengths—10 mm, 20 mm, and 40 mm—the experimental results maintain overall consistency with simulation trends. From bending angle experimental data, although the 10 mm actuator exhibits the strongest bending response, its curve linearity is slightly inferior to the 20 mm configuration, particularly showing slight nonlinear elevation in the medium-high pressure range above 0.03 MPa, related to material nonlinear response from local stress concentration under end cap constraint in short actuators. The 40 mm actuator shows recovery at high pressure, but exhibits more obvious response hysteresis at low pressure with noticeable lag phenomena during pressurization–depressurization cycles, directly related to its larger air chamber volume. In contrast, the 20 mm actuator demonstrates near-perfect linear relationships between bending angle and axial elongation with gas pressure across the entire 0.01–0.04 MPa test range.

This experimental result further confirms that 20 mm is not merely a compromise selection at the simulation level, but likewise exhibits optimal controllability and predictability on the actual physical prototype. On one hand, its response curve demonstrates the best linearity, meaning subsequent open-loop or closed-loop control can directly employ simplified linear mapping relationships without requiring additional compensation for nonlinear segments, significantly reducing the modeling complexity of wall-climbing robot gait control algorithms. On the other hand, its pressurization–depressurization response consistency and repeatability are superior, indicating that the actuator at this length possesses better fatigue stability and batch consistency, better satisfying wall-climbing robot requirements for joint motion reliability during long-term continuous operation. Combining the dual results of simulation optimization and experimental validation, the 20 mm actuator possesses excellent driving performance, optimal model conformance accuracy, and strongest engineering feasibility, ultimately being determined as the preferred effective length of the soft actuator in this study, serving as the standard configuration for subsequent wall-climbing robot prototype integration and application validation.

In summary, the high-level consistency of theoretical modeling, finite element simulation, and physical experiment results fully validates that the proposed three-chamber pneumatic bellows soft actuator with an optimized configuration of 20 mm length, two-layer structure, and YG-G15 material possesses comprehensive advantages including low-pressure actuation, bending-elongation decoupled control, and excellent linear response characteristics, demonstrating engineering feasibility as a flexible joint unit for wall-climbing

robots. The following section will further explore integration methods of this actuator in wall-climbing robot systems and verify its actual motion performance under complex wall surface conditions.

5. Discussion

5.1. Limitations and Future Work

5.1.1. On the Compliance–Rigidity Trade-Off Under Representative Loading Conditions

The structural comparisons in Section 3.1 (bellows layer number) and the resulting selection of the two-layer configuration were based on finite element simulations under pneumatic loading alone, without external gravitational or contact loads representative of actual wall-attachment operation. As such, the present results do not directly establish the actuator's structural rigidity margin, nor the minimum bending/elongation compliance required for reliable conformity to representative wall curvatures, under combined pneumatic and external loading. In general, structural load-bearing rigidity and passive wall-conformity compliance constitute a design trade-off; a rigorous treatment would formulate this as a multi-objective structural optimization problem over bellows layer number, wall thickness, and effective length, subject to safety-factor and target-compliance constraints derived from the intended climbing surface geometry and robot payload. Incorporating representative external loading into the finite element model and formally solving this optimization problem are identified as necessary directions for future work.

5.1.2. On the Experimental Validation Scope of the Decoupled Model

The experimental campaign in Section 4 was designed around two boundary parameter configurations (pure elongation and single-chamber bending) rather than the full three-dimensional pressure space (p_1, p_2, p_3). Consequently, the decoupling property between elongation and bending—the central claim motivating the analytical model of Section 2—has been validated only along these two boundaries, not under simultaneous combined actuation. A representative future test matrix would apply several combinations of unequal chamber pressures spanning both the elongation and bending ranges characterized in this study, with simultaneous measurement of ΔL, φ, and θ for direct comparison against Equations (4), (8) and (14).

5.1.3. On the Influence of Hydrostatic Water Pressure on Modeling and Performance

Since the proposed soft actuator is conceptualized for wall-climbing robots in marine or petrochemical vessel environments, the influence of external hydrostatic pressure P_{est} on the mechanical model and physical performance must be considered for underwater deployment.

Mathematically, the driving force of the bellows relies on the differential pressure $\Delta p = p_{in} - P_{est}$. In submerged conditions at depth □, the external pressure scales as $P_{est} = P_{atm} + \rho g h$. Consequently, the input terms p_i in the analytical models for axial elongation (Equation (4)) and bending (Equation (14)) must be replaced by the effective differential pressure $\Delta p_i = p_i - \rho g h$. To achieve equivalent deformation underwater, a higher absolute supply pressure is required to overcome the hydrostatic preload.

Structurally, high hydrostatic pressure exerts compressive loads on the hyperelastic bellows walls, potentially causing radial contraction of the inner bore area S_i and increasing the effective bending stiffness of the silicone structure. Furthermore, operating in water introduces significant added mass and viscous damping compared to air, which will damp high-frequency motions and increase the transient response time during inflation and deflation cycles.

Incorporating a depth-dependent hydrostatic correction term into the analytical formulation and conducting high-pressure chamber tests remain crucial directions for our future work.

6. Conclusions

To address the limitations of existing pneumatic soft actuators regarding insufficient degrees of freedom, severe coupling, and poor output linearity, this study designed a three-chamber pneumatic bellows soft actuator tailored for soft wall-climbing robot applications. Systematic mechanical modeling, finite element simulation optimization, and prototype experimental verification were conducted. The main conclusions are as follows:

(1) A three-parameter decoupled mechanical model was established. Based on the constant-curvature assumption and Euler–Bernoulli beam theory, analytical models encompassing axial elongation, bending direction, and bending angle were derived, clarifying the independent control variables for each: axial elongation is solely determined by the average pressure of the three chambers, bending direction is solely determined by the pressure ratio among the three chambers, and bending angle is determined by the balance between driving torque and structural impedance torque. This model theoretically validates that the three motion parameters can achieve mutual decoupling and independent regulation, providing a theoretical foundation for precise actuator control.

(2) The influence pattern of bellows layer number on driving performance was clarified. Finite element simulation results show that under identical pressure, the safety factor of the two-layer bellows structure is increased to 33.44, while axial displacement is approximately 32.2% higher. Comprehensive displacement-stress efficiency index analysis shows the efficiency of the two-layer structure is approximately 2.88 times that of the three-layer structure. Therefore, under pneumatic loading conditions, the two-layer bellows structure exhibits clear advantages in structural safety and driving efficiency and was selected as the prototype configuration; its structural reliability under combined pneumatic and external wall-attachment loading remains to be established through the future optimization study discussed in Section 5.1.

(3) Through systematic comparison of three effective lengths—10 mm, 20 mm, and 40 mm—the optimal structural parameters balancing linear response and engineering applicability were determined. Simulation results show that bending angle is not a monotonic function of length, but rather results from the coupled action of end moment arm and structural relative rigidity; axial elongation is approximately proportional to length. Simulation-experiment relative errors for the three lengths are overall comparable: the average error of bending angle ranges from 11.8% to 12.6%, and the average error of elongation ranges from 10.4% to 12.1%. However, further analysis of error variation trends with pressure reveals that the 10 mm actuator shows increasing rather than decreasing relative errors as actual working pressure is approached, while the 40 mm actuator exhibits obvious nonlinear response jumps in the medium-high pressure range, both reflecting insufficient prediction accuracy or response stability under high-pressure large-deformation conditions. The 20 mm actuator's relative error shows convergence in this pressure range, with bending angle and axial elongation varying approximately linearly with pressure without discontinuities, indicating higher predictive reliability of its simulation model at actual working pressures and easier modeling and control of its response. Material hardness comparison shows that low-hardness YG-G15 silicone produces larger bending angle and axial elongation compared to YG-E630, making it the superior actuator fabrication material.

(4) Prototype fabrication and experimental verification were completed, confirming the validity of the model and structural selection. A pneumatic experimental platform was established to conduct bending and elongation characteristic experiments for actuators of three lengths (10 mm, 20 mm, 40 mm) fabricated from YG-G15 material. Results show that experimental data at each length are overall in good agreement with theoretical models and simulation results. Notably, the 20 mm actuator not only demonstrates advantages in error convergence and response linearity at the simulation level but also validates this conclusion in physical-prototype experiments: its bending angle and axial elongation exhibit near-perfect linear relationships with pressure across the entire 0.01–0.04 MPa working pressure range, the maximum relative error in the bending angle is 14%, and the maximum relative error in the elongation is 12.5%. Additionally, its pressurization–depressurization response consistency and repeatability are superior to both 10 mm and 40 mm configurations, indicating that the actuator at this length possesses good fatigue stability and batch consistency. This demonstrates that 20 mm is not merely a compromise selection at the simulation level, but rather the optimal engineering configuration verified at theoretical, simulation, and experimental levels.

Furthermore, back-calibration of the axial compliance coefficient α confirms that the analytical model (Equation (16)) is reliable only within the low-pressure regime (0.01–0.02 MPa, relative error $\approx$ 0%), with error increasing to 25–38.5% at higher pressures (0.03–0.04 MPa) due to material and geometric nonlinearity—consistent with the FE simulation error trends discussed above.

It should be explicitly noted that the present study does not involve dynamic underwater wall-climbing validation; all experimental results reported here were obtained under dry (on-land) conditions. The actuator is designed with underwater wall-climbing applications (e.g., ship-hull and offshore-structure inspection) as a target scenario, rather than a fully validated underwater capability at this stage. Genuine underwater wall-climbing experiments constitute a key direction of our subsequent work, as detailed in Section 5.1.

In summary, the proposed three-chamber pneumatic bellows soft actuator, under the optimized configuration of two-layer structure, 20 mm length, and YG-G15 material, can achieve continuous, controllable, decoupled actuation of bending direction, bending angle, and axial elongation within a low-pressure range of 0.01–0.04 MPa, combining excellent response linearity, model reliability, and engineering feasibility. Future work will focus on actuator dynamics modeling, closed-loop control strategy design, and multi-joint coordinated gait planning, further validating its motion performance in practical scenarios such as complex curved surface wall-climbing and narrow pipe inspection.

Author Contributions: Conceptualization, L.Y. and L.Z.; Methodology, L.Y. and L.Z.; Software, L.Y.; Validation, L.Y., L.Z. and L.Y. and F.S.; Formal analysis, L.Y. and L.Z.; Investigation, L.Y.; Resources, L.Y. and L.Z.; Data curation, L.Y. and L.Z.; Writing—original draft, L.Y.; Writing—review and editing, L.Z. All authors have read and agreed to the published version of the manuscript.

Funding: This work was supported by the National Natural Science Foundation of China (Grant No. 52265013).

Data Availability Statement: The data presented in this study are available on request from the corresponding author.

Conflicts of Interest: The authors declare that the research was conducted in the absence of any commercial or financial relationships that could be construed as a potential conflict of interest.

References

1. Rus, D.; Tolley, M.T. Design, fabrication and control of soft robots. *Nature* **2015**, *521*, 467–475. [CrossRef] [PubMed]
2. Xavier, M.S.; Tawk, C.D.; Fleming, A.; Zolfagharian, A.; Pinskier, J.; Howard, D.; Young, T.; Lai, J.; Harrison, S.M.; Yong, Y.K. Soft Pneumatic Actuators: A Review of Design, Fabrication, Modeling, Sensing, Control and Applications. *IEEE Access* **2022**, *10*, 59442–59485. [CrossRef]
3. Mosadegh, B.; Polygerinos, P.; Keplinger, C.; Wennstedt, S.; Shepherd, R.; Gupta, U.; Shim, J.; Bertoldi, K.; Walsh, C.J.; Whitesides, G.M. Pneumatic Networks for Soft Robotics that Actuate Rapidly. *Adv. Funct. Mater.* **2014**, *24*, 2163–2170. [CrossRef]
4. Guan, Q.; Sun, J.; Liu, Y.; Wereley, N.M.; Leng, J. Novel Bending and Helical Extensile/Contractile Pneumatic Artificial Muscles Inspired by Elephant Trunk. *Soft Robot.* **2020**, *7*, 597–614. [CrossRef] [PubMed]
5. Connolly, F.; Polygerinos, P.; Walsh, C.J.; Bertoldi, K. Mechanical Programming of Soft Actuators by Varying Fiber Angle. *Soft Robot.* **2015**, *2*, 26–32. [CrossRef]
6. Colucci, G.; Duretto, S.; Tagliavini, L.; Botta, A.; Quaglia, G. A bi-directional pneumatic actuator for sustainable robotic systems. *Sens. Actuators A Phys.* **2025**, *393*, 116800. [CrossRef]
7. Ranzani, T.; Gerboni, G.; Cianchetti, M.; Menciassi, A. A bioinspired soft manipulator for minimally invasive surgery. *Bioinspir. Biomim.* **2015**, *10*, 035008. [CrossRef] [PubMed]
8. Gong, Z.; Fang, X.; Chen, X.; Cheng, J.; Xie, Z.; Liu, J.; Chen, B.; Yang, H.; Kong, S.; Hao, Y.; et al. A soft manipulator for efficient delicate grasping in shallow water: Modeling, control, and real-world experiments. *Int. J. Robot. Res.* **2020**, *40*, 449–469. [CrossRef]
9. Yang, P.; Sun, L.; Zhang, M. Design and analysis of a passive adaptive wall-climbing robot on variable curvature ship facades. *Appl. Ocean Res.* **2024**, *143*, 103879. [CrossRef]
10. Shahrami, M.; Khorasanchi, M. Development of a Climbing Robot for Ship Hull Inspection. *J. Surv. Fish. Sci.* **2023**, *10*, 1–11.
11. Zang, G.; Dai, Z.; Li, Y. Soft Gecko-shaped Tail with Passive Auto-reset Joint Enhances the Locomotion in Gecko-inspired Climbing Robots. *J. Bionic Eng.* **2025**, *22*, 83–95. [CrossRef]
12. Chen, R.; Tao, X.; Cao, C.; Jiang, P.; Luo, J.; Sun, Y. A soft, lightweight flipping robot with versatile motion capabilities for wall-climbing applications. *IEEE Trans. Robot.* **2023**, *39*, 3960–3976. [CrossRef]
13. Tan, Y.J.; Mengaldo, G.; Laschi, C. Artificial Muscles for Underwater Soft Robots: Materials and Their Interactions. *Annu. Rev. Condens. Matter Phys.* **2024**, *15*, 45–61. [CrossRef]
14. Zhang, Z.; Wang, X.; Wang, S.; Meng, D.; Liang, B. Design and Modeling of a Parallel-Pipe-Crawling Pneumatic Soft Robot. *IEEE Access* **2019**, *7*, 7134301–7134317. [CrossRef]
15. Webster, J.R.; Jones, B.A. Design and Kinematic Modeling of Constant Curvature Continuum Robots: A Review. *Int. J. Robot. Res.* **2010**, *29*, 1661–1683. [CrossRef]
16. Shapiro, Y.; Gabor, K.; Wolf, A. Modeling a Hyperflexible Planar Bending Actuator as an Inextensible Euler–Bernoulli Beam for Use in Flexible Robots. *Soft Robot.* **2015**, *2*, 71–79. [CrossRef]
17. Polygerinos, P.; Wang, Z.; Overvelde, B.J.T.; Galloway, K.C.; Wood, R.J.; Bertoldi, K.; Walsh, C.J. Modeling of Soft Fiber-Reinforced Bending Actuators. *IEEE Trans. Robot.* **2015**, *31*, 778–789. [CrossRef]
18. Falkenhahn, V.; Mahl, T.; Hildebrandt, A.; Neumann, R.; Sawodny, O. Dynamic Modeling of Bellows-Actuated Continuum Robots Using the Euler-Lagrange Formalism. *IEEE Trans. Robot.* **2015**, *31*, 1483–1496. [CrossRef]
19. Elsayed, Y.; Vincensi, A.; Lekakou, C.; Geng, T.; Saaj, C.M.; Ranzani, T.; Cianchetti, M.; Menciassi, A. Finite Element Analysis and Design Optimization of a Pneumatically Actuating Silicone Module for Robotic Surgery Applications. *Soft Robot.* **2014**, *1*, 255–262. [CrossRef]
20. Chen, C.; Liang, Y.; Sun, J.; Lin, C.; Wen, Y. Adaptive pneumatic soft gripper with embedded flexible bending sensor. *Ind. Robot Int. J. Robot. Res. Appl.* **2024**, *51*, 358–368. [CrossRef]
21. Yin, J.; Zhang, D.; Xu, Z.; Fan, W.; Xia, Y.; Sui, K. Precisely Controlling the Output Force of Hydrogel Actuator Based on Thermodynamic Nonequilibrium Temporary Deformation. *ACS Appl. Mater. Interfaces* **2020**, *12*, 49042–49049. [CrossRef] [PubMed]
22. Ma, H.; Zhou, J. Modeling, Characterization, and Application of Soft Bellows-Type Pneumatic Actuators for Bionic Locomotion. *Acta Mech. Solida Sin.* **2022**, *36*, 1–12. [CrossRef]
23. Abboodi, M.; Doumit, M. Design, manufacturing, and testing of a novel omnidirectional soft sleeve actuator. *Sci. Rep.* **2026**, *16*, 9828. [CrossRef] [PubMed]
24. Zhang, L.; Meng, W.; Ni, G.; Ma, K.; Xu, F. Research on bending performance and control of Pneu-net type variable-curvature soft actuator. *Chin. J. Sci. Instrum.* **2024**, *45*, 321–334.
25. Zhang, L.; Zhang, J.; Meng, W. Modeling and deformation characteristics of pneumatic bellows actuator. *Chin. J. Sci. Instrum.* **2025**, *46*, 188–203.

Disclaimer/Publisher's Note: The statements, opinions and data contained in all publications are solely those of the individual author(s) and contributor(s) and not of MDPI and/or the editor(s). MDPI and/or the editor(s) disclaim responsibility for any injury to people or property resulting from any ideas, methods, instructions or products referred to in the content.